CENTER FOR CONNECTED AND AUTOMATED TRANSPORTATION

AWD-001401
July 2026

Roadway Friction Screening and Measurement with Automated Vehicle Telematics and Control

Xiaopeng (Shaw) Li, PhD
Yanfeng Ouyang, PhD
Zhaohui Liang, PhD
Caio Beojone, PhD
Heye Huang, PhD

WISCONSIN
UNIVERSITY OF WISCONSIN–MADISON

ILLINOIS CENTER FOR TRANSPORTATION

CENTER FOR CONNECTED AND AUTOMATED TRANSPORTATION

Report No. AWD-001401
Project Start Date: 07/01/2024
Project End Date: 12/31/2025

September 2025

Roadway Friction Screening and Measurement with Automated Vehicle Telematics and Control

by
Xiaopeng (Shaw) Li, Professor
University of Wisconsin - Madison
Yanfeng Ouyang, Professor
University of Illinois at Urbana - Champaign

DISCLAIMER

Funding for this research was provided by the Center for Connected and Automated Transportation under Grant No. 69A3551747105 of the U.S. Department of Transportation, Office of the Assistant Secretary for Research and Technology (OST-R), University Transportation Centers Program. The contents of this report reflect the views of the authors, who are responsible for the facts and the accuracy of the information presented herein. This document is disseminated under the sponsorship of the Department of Transportation, University Transportation Centers Program, in the interest of information exchange. The U.S. Government assumes no liability for the contents or use thereof.

Suggested APA Format Citation: Li, X., Ouyang, Y., Liang, Z., Beojone, C., Huang, H. (2026). Roadway Friction Screening and Measurement with Automated Vehicle Telematics and Control (Report No. AWD-001401). University of Wisconsin-Madison. Illinois Center for Transportation.

Contacts

For more information:

Xiaopeng (Shaw) Li
University of Wisconsin-Madison
1415 Engineering Drive Madison, WI 53706
Phone: 608-890-0104
Email: xli2485@wisc.edu

Yanfeng Ouyang
University of Illinois at Urbana - Champaign
1209 Newmark Civil Engineering Bldg
Phone: 217-333-9858
Email: yfouyang@illinois.edu

CCAT
University of Michigan Transportation Research Institute
2901 Baxter Road
Ann Arbor, MI 48109
umtri-ccat@umich.edu
(734) 763-2498

CENTER FOR CONNECTED AND AUTOMATED TRANSPORTATION

Technical Report Documentation Page

1. Report No. AWD-001401	**2. Government Accession No.** Leave blank - not used	**3. Recipient's Catalog No.** Leave blank - not used
4. Title and Subtitle Roadway Friction Screening and Measurement with Automated Vehicle Telematics and Control		**5. Report Date** September 2025 **6. Performing Organization Code** LCLSJAGTNZQ7
7. Author(s) Xiaopeng (Shaw) Li, Ph.D.: https://orcid.org/0000-0002-5264-3775 Yanfeng Ouyang, Ph.D.: https://orcid.org/0000-0002-5944-2044 Zhaohui Liang, Ph.D.: https://orcid.org/0000-0002-3357-9309 Caio Beojone, Ph.D.: https://orcid.org/0000-0002-6491-7104 Heye Huang, Ph.D.: https://orcid.org/0000-0002-8964-8764		**8. Performing Organization Report No.** Enter any/all unique alphanumeric report numbers assigned by the performing organization, if applicable.
9. Performing Organization Name and Address University of Wisconsin - Madison 500 Lincoln Dr, Madison, WI 53706 University of Illinois at Urbana - Champaign 506 S. Wright St. Urbana, IL 61801-3633		**10. Work Unit No.** **11. Contract or Grant No.** Contract No. GR000036376 UWMSN | Shaw_CCAT_YR2_Connected Intel (AAN9211)
12. Sponsoring Agency Name and Address U.S. Department of Transportation Office of the Assistant Secretary for Research and Technology 1200 New Jersey Avenue, SE Washington, DC 20590		**13. Type of Report and Period Covered** Final Report(July 2024 - December 2025) **14. Sponsoring Agency Code** OST-R
15. Supplementary Notes Conducted under the U.S. DOT Office of the Assistant Secretary for Research and Technology's (OST-R) University Transportation Centers (UTC) program.		

1. Report No.	2. Government Accession No.	3. Recipient's Catalog No.
Enter the report number assigned by the sponsoring agency.	Leave blank - not used	Leave blank - not used

16. Abstract

Accurate estimation of the tire-road friction coefficient (TRFC) is essential for ensuring safe vehicle control, particularly under adverse road conditions. Conventional approaches typically rely on naturalistic driving data from regular vehicles, which operate under mild acceleration and braking and therefore provide limited slip excitation and insufficient observability of peak TRFC. To address this limitation, we developed a high-slip-ratio control framework that enables automated vehicles (AVs) to actively excite the peak friction region during empty-haul operations while maintaining operational safety. The framework employs a simplified Magic Formula tire model to capture nonlinear slip-force dynamics, locally fitted through repeated high-slip measurements. To ensure safety in car-following scenarios, we designed a constrained optimal control strategy that balances slip excitation, trajectory tracking, and collision avoidance. In addition, a binning-based statistical projection method was introduced to robustly estimate peak TRFC in the presence of noise and local data sparsity. To further improve estimation accuracy, we also developed a network routing method that leverages spatial information from multiple vehicles and routes. The complete framework was validated through closed-loop simulations and real-vehicle experiments, demonstrating its accuracy, robustness, safety, and scalability for cost-effective roadway friction screening.

17. Key Words	18. Distribution Statement
Friction estimation; High-slip-ratio control; Automated vehicles; Network operation	No restrictions.

19. Security Classif. (of this report)	20. Security Classif. (of this page)	21. No. of Pages	22. Price
Unclassified	Unclassified	Enter the total number of pages in the report, including both sides of all pages and the front and back covers.	Leave blank - not used

Form DOT F 1700.7 (8-72) Reproduction of completed page authorized

Table of Content

S

List of Figures

CENTER FOR CONNECTED AND AUTOMATED TRANSPORTATION

Project abstract

Accurate estimation of the tire-road friction coefficient (TRFC) is essential for ensuring safe vehicle control, particularly under adverse road conditions. Conventional approaches typically rely on naturalistic driving data from regular vehicles, which operate under mild acceleration and braking and therefore provide limited slip excitation and insufficient observability of peak TRFC. To address this limitation, we developed a high-slip-ratio control framework that enables automated vehicles (AVs) to actively excite the peak friction region during empty-haul operations while maintaining operational safety. The framework employs a simplified Magic Formula tire model to capture nonlinear slip-force dynamics, locally fitted through repeated high-slip measurements. To ensure safety in car-following scenarios, we designed a constrained optimal control strategy that balances slip excitation, trajectory tracking, and collision avoidance. In addition, a binning-based statistical projection method was introduced to robustly estimate peak TRFC in the presence of noise and local data sparsity. To further improve estimation accuracy, we also developed a network routing method that leverages spatial information from multiple vehicles and routes. The complete framework was validated through closed-loop simulations and real-vehicle experiments, demonstrating its accuracy, robustness, safety, and scalability for cost-effective roadway friction screening.

1. Introduction

In adverse weather conditions such as rain, snow, or ice, insufficient tire-road adhesion is a major contributor to vehicle skidding, extended braking distances, and loss of control, significantly increasing crash risk [1], [2], [3]. Accurate estimation of the tire-road friction coefficient (TRFC) is therefore critical for enhancing traffic safety and supporting infrastructure asset management[4]. Despite this, federal and local agencies continue to report limited information on pavement management systems [3]. Furthermore, as a core parameter in both longitudinal and lateral vehicle dynamics, the peak TRFC defines the maximum traction available and plays a decisive role in acceleration, braking, and stability control [5], [6].

Current TRFC estimation approaches can be broadly categorized into two groups: (1) skidding-based estimation, and (2) vehicle-based estimation using onboard sensors. The skidding-based estimation employs mechanical friction testers, such as the Locked-Wheel Skid Trailer (LWST), Mu-Meter, and Sideway-force Coefficient Routine Investigation Machine (SCRIM), are commonly used by road agencies to quantify pavement friction. [7], [8]These devices induce slip through controlled mechanisms to directly measure tire-road interaction. While highly accurate in controlled settings, their deployment is limited by cost, operational complexity, and inability to provide continuous or geometry-flexible measurements (e.g., on ramps or curves) [9], [10]. For instance, LWST simulates full sliding using a locked test wheel, and SCRIM uses a yawed tire but requires frequent recalibration and cannot easily navigate complex road geometries. Skidding-based methods also demand delicate, costly, and specialized equipment and vehicles, resulting in substantial expenses for transportation authorities and restricting updates to measurement campaigns that are typically conducted only annually, biannually, or even less frequently.

Vehicle-based estimation methods infer TRFC indirectly from onboard sensor data, such as wheel speeds, inertial measurements (IMUs), global positioning system (GPS), and brake signals. These methods offer greater scalability than mechanical testers and are compatible with modern connected or autonomous vehicle platforms. They can be broadly divided into regression-based and learning-based approaches.

Regression-based methods rely on simplified physical models of vehicle dynamics (e.g., 1-DOF, bicycle, or 3-DOF models) combined with empirical or semi-empirical tire models, such as the Magic Formula, brush model, or Burckhardt model [11], [12], [13]. These models typically use measured accelerations, forces, and slip ratios, to estimate friction, where the slip ratio refers to the relative difference between tire rotational speed and vehicle speed. However, under naturalistic driving, vehicles operate at low slip ratios (e.g., $\kappa < 0.05$), which are insufficient to capture the nonlinear regime near peak TRFC. Furthermore, many such models assume constant vertical loads and neglect dynamic load transfer during aggressive maneuvers [14], [15], leading to biased or conservative estimates.

Learning-based methods extend beyond the assumptions of physical models by training machine learning algorithms, such as neural networks, support vector machines, time series analysis [16] and deep architectures (CNNs [17], LSTMs [18], and Transformers [19]), to map sensor data directly to TRFC estimates. Some also incorporate visual features from onboard cameras to infer road texture and surface condition [20]. While these models can capture complex nonlinearities, their performance heavily depends on the diversity of the training data. Critically, the scarcity of high-slip samples in naturalistic datasets limits their ability to generalize to peak TRFC conditions. Moreover, the lack of physical interpretability raises concerns in safety-critical applications.

To improve robustness, many of these methods are extended via multi-sensor fusion frameworks that combine inputs from vision, inertial, and brake systems using Kalman filtering (e.g., EKF, UKF, CKF) or observer-based methods [21], [22].Recent studies have also explored road classification using ABS-induced brake pressure pulses [23]. While these hybrid techniques enhance noise filtering and environmental adaptation, they remain fundamentally passive and rely on ambient driving behaviors. As a result, they often fail to induce the high-slip conditions necessary to observe peak friction, producing only lower-bound estimates.

To address these limitations, we propose a novel high-slip-ratio control and estimation framework that actively excites tire-road interaction using automated vehicles (AVs) during empty-haul operations. By leveraging the operational flexibility of AVs, controlled acceleration and deceleration maneuvers enable safe and repeatable access to high-slip regimes-even under worst-case assumptions-conditions that conventional regular vehicles (RVs) cannot achieve due to safety and comfort constraints. To support this, a computationally efficient tire model derived from the Magic Formula, validated through sensitivity analysis, is used alongside a binning-based statistical projection method to robustly estimate peak tire-road friction coefficients (TRFCs) from high-slip data. A constrained optimal control strategy ensures safe slip excitation while maintaining car-following safety constraints. The overall effectiveness of this framework is validated through closed-loop simulations and on-road field experiments, highlighting its accuracy, robustness, and scalability.

Building on this high-fidelity estimation capability, we extend the approach to a network-wide dynamic strategy that integrates measurements from both controlled AVs and uncontrolled RVs. While RVs provide broad but low-precision data, AVs are guided dynamically through a rolling-horizon routing and covering problem, solved efficiently via a Branch-and-Price algorithm, to target the most critical points in the network. This framework incorporates a comprehensive statistical pipeline that aggregates multi-source pavement friction data, performs non-linear regression and data fusion, and quantifies the impact of misestimation. As a result, the road network-characterized by limited knowledge of TRFCs-is continuously updated and enriched by the combined contributions of RVs and AVs.

Together, these efforts establish an end-to-end pavement friction assessment pipeline that couples advanced AV-based control strategies with dynamic network-level integration. The key contributions include: (i) an active high-slip-ratio excitation strategy with AVs during empty-haul trips for accurate peak TRFC estimation; (ii) a constrained optimal control design balancing slip excitation, safety, and trajectory tracking; (iii) a statistical framework for multi-source friction data fusion and misestimation analysis; (iv) an efficient routing and covering algorithm for AV deployment within a rolling-horizon framework; and (v) extensive validation through both real-world field experiments and a simulated case study in Champaign County, demonstrating scalability to larger networks.

2. Methodology

Accurate estimation of the peak Tire-Road Friction Coefficient (TRFC) requires intentional excitation of the high-slip regime, which is generally inaccessible under normal driving conditions. To address this challenge, this section presents a simplified tire model, a statistical projection-based estimator, and a high-slip-ratio control framework tailored for autonomous vehicles (AVs). The proposed approach enables interpretable TRFC estimation while ensuring operational safety in realistic car-following scenarios.

In longitudinal vehicle dynamics, the TRFC exhibits a nonlinear dependence on the slip ratio. At low slip ratios (typically below 0.1), the TRFC rises sharply and reaches its maximum at the critical slip ratio (CSR). Beyond the CSR, it gradually decreases and stabilizes at a lower, quasi-constant level. The magnitude of the peak TRFC depends strongly on tire and pavement characteristics, including tire composition and surface conditions. However, under everyday driving, vehicles rarely operate at slip ratios high enough to approach this peak. Most slip ratios remain below 0.05, restricting access to the high-friction region and limiting opportunities to fully capture the TRFC profile.

Direct measurement methods, such as skid testers or instrumented trailers, can provide accurate data but are costly and impractical for large-scale or real-time deployment. These limitations hinder both model-based and learning-based estimation methods, which often lack reliable peak friction data for calibration or training.

To overcome this issue, we propose a slip-ratio control strategy that deliberately induces high-slip conditions under controlled, safe maneuvers. Moreover, we mathematically demonstrate that, assuming a fixed CSR, higher instantaneous vehicle acceleration reduces the prediction error of peak TRFC. This methodology provides reliable access to high-friction data and facilitates interpretable, data-driven friction estimation under real-world constraints.

2.1. Definition of slip ratio

The slip ratio κ quantifies the relative longitudinal motion between a vehicle's tire and the road surface, serving as a key variable in characterizing tire force generation. Its definition varies depending on whether the vehicle is accelerating or braking. However, to ensure consistency and applicability across different driving modes, we adopt the following unified formulation:

$$\kappa = \frac{V_{wheel} - V_{vehicle}}{max\left(V_{vehicle}, \epsilon\right)} \quad (1)$$

Where, $V_{wheel} = \omega \cdot R_e$ is the tangential velocity at the tire circumference, computed from the wheel angular velocity ω and the effective rolling radius $R_e \cdot V_{vehicle}$ denotes the vehicle's longitudinal velocity measured at the center of gravity. A small positive constant ϵ is included in the denominator to prevent division by zero and ensure numerical stability during low-speed or standstill conditions. This normalized definition allows for seamless integration into the tire force model in Section 2.2 and the slip-ratio-based control strategy introduced later in Section 2.5. Notably, positive slip ratios $\kappa > 0$ typically correspond to driving or acceleration scenarios, while negative values reflect braking or wheel lockup conditions.

2.2. Vehicle dynamic model

To account for variations in longitudinal tire forces due to vertical load transfer, slope, and aerodynamic drag, we model the vehicle as a four-wheel system, as illustrated in Figure 1. The longitudinal dynamics follow Newton's second law:

$$m a_y = \sum_{i \in \{F,R\}, j \in \{L,R\}} F_{yij} - F_{dy} - mgsin(\gamma) \qquad (2)$$

where m is the vehicle mass, a_y is the longitudinal acceleration of the center of gravity (CG), F_{yij} denotes the longitudinal tire force at wheel ij ($i \in \{F,R\}$ for front/rear and $j \in \{L,R\}$ for left/right), $F_{dy} = \frac{1}{2} \rho C_d A_f v^2$ is the aerodynamic drag, and γ is the road slope angle.

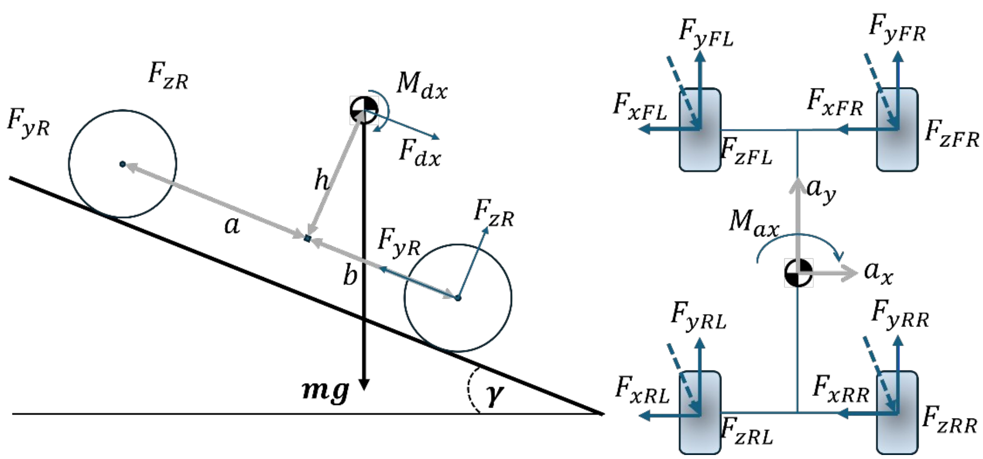

Figure 1 Four-wheel Vehicle Model Considering Slope

The dynamic normal load on each axle is affected by pitch motion and CG height:

$$F_{zF} = \frac{mg}{2L}\left(b - h\frac{a_y}{g}\right) \qquad (3)$$

$$F_{zR} = \frac{mg}{2L}\left(a + h\frac{a_y}{g}\right) \qquad (4)$$

where a and b are the longitudinal distances from CG to the front and rear axles, respectively, $L = a + b$ is the wheelbase, and h is the CG height. F_{zF} and F_{zR} denote the total normal loads on the front and rear axles. This model enables accurate estimation of slip ratios and tire forces under dynamic conditions. Each longitudinal tire force F_{yij} is computed as $F_{yij} = \mu_{ij} \cdot F_{zij}$, where the friction coefficient μ_{ij} depends on the slip ratio κ_{ij}.

2.3. Magic formula

The Magic Formula (MF) is a widely adopted empirical model [24] for capturing the nonlinear relationship between tire forces and slip, both in the longitudinal and lateral directions. Due to its excellent performance across a wide range of conditions, it is commonly referred to as the "Magic Formula." In this study, we focus exclusively on modeling the longitudinal tire force, which is expressed as:

$$\mu\left(\kappa \middle| \mu^{max}, \beta_1, \beta_2, \beta_3\right) = \mu^{max} \sin\left(\beta_2 \arctan\left(\beta_1 \kappa - \beta_3 \cdot \left(\beta_1 \kappa - \arctan\left(\beta_1 \kappa\right)\right)\right)\right) \tag{5}$$

where $\mu^{max}, \beta_1, \beta_2, \beta_3$ are empirical parameters used to fit the model to experimental data. Among these parameters, $\mu^{max}$is the primary output of interest. It is easy to show that the product $\mu^{max}\beta_1\beta_2$ gives the slope of the curve $d\mu/d\kappa$ near the origin (as $\kappa \to 0$). Also, first-order condition shows that the peak friction is achieved when κ satisfies the following:

$$\frac{\partial \mu\left(\kappa \vee \hat{\mu}^{max}, \beta_1, \beta_2, \beta_3\right)}{\partial \kappa} = \frac{\beta_2 \mu^{max} \cos\left(\phi\right) \psi}{\left(\beta_1 \kappa - \beta_3 \cdot \left(\beta_1 \kappa - \arctan\left(\beta_1 \kappa\right)\right)\right)^2 + 1} = 0 \tag{6}$$

Where $\phi = \beta_2 \arctan\left(\beta_1 \kappa - \beta_3\left(\beta_1 \kappa - \arctan\left(\beta_1 \kappa\right)\right)\right)$, and $\psi = \beta_1 - \beta_3\left(\beta_1 - \frac{\beta_1}{\beta_1^2 \kappa^2 + 1}\right)$. Therefore, the critical slip ratio simply satisfies $\cos\left(\phi\right) = 0$ or $\psi = 0$. Since the MF is an odd function of κ, the solution to Equation $\left(6\right)$ is unique for $\kappa \geq 0$ if $\beta_2 \arctan\left(\beta_1 - \beta_3\left(\beta_1 - \arctan\left(\beta_1\right)\right)\right) \leq 3\pi/2$, a condition trivially satisfied in practice [11], [24].

2.4. Error measurement of prediction

For a discrete data collection system, and in the absence of prior knowledge of the simplified Magic Formula tire model, we estimate the maximum tire-road friction coefficient (TRFC) independently at each sampled time point. Assuming a fixed critical slip ratio (CSR) by selecting a constant parameter β_1, we locally fit the simplified Magic Formula using observed data and nonlinear optimization.

Specifically, we apply a bounded optimization method (e.g., MATLAB's *fmincon*) to identify the best-fitting parameters β_2 and μ^{max} at each time step by minimizing the difference between the measured longitudinal force and the model prediction. This point-wise fitting process yields a set of local TRFC estimates.

Because the optimization is performed independently at each point and relies on limited local measurements, the resulting Max-TRFC estimates may exhibit variability due to sensor noise, data sparsity, and local fitting uncertainty, as illustrated in Figure 2. To quantify this variability, we define an error term as follows:

- Aggregate the data based on slip ratio for error analysis. Define a set of bins I with a bin width of 0.01, covering the range from 0.01 to 0.3.

- For each bin $i \in I$, define the set of predicted peak TRFC value as $y_i := \{y_{ij}\}_{j \in J_i}$ where each y_{ij} is an individual prediction within bin i.
- Let $y := U_{i \in I\, y_i}$ denote the set of all predicted peak TRFC value across all bins.
- Let $\bar{y}$ denote the true or referenced peak TRFC value.
- The sample mean of predicted peak TRFC value in bin i is defined as: $\hat{y}_i := \frac{1}{¿ J_i \vee ¿ \sum_{j \in J} y_{ij} ¿}$
- Let $\delta_i := STD(\hat{y}_i)$ denote the standard deviation of prediction in bin i and $\bar{y}_i := E(\hat{y}_i)$ be the empirical expectation.
- Define the mean squared error for bin i with respect to the true peak TRFC as $e_i = E(y_{ij} - \bar{y})^2$

Using the bias-variance decomposition, the mean squared error term e_i can be rewritten as:

$$e_i = \frac{1}{|J_i|} \sum_{j \in J_i} (y_{ij} - \hat{y}_i)^2 + ¿(\hat{y}_i - \bar{y})^2 ¿ \qquad (7)$$

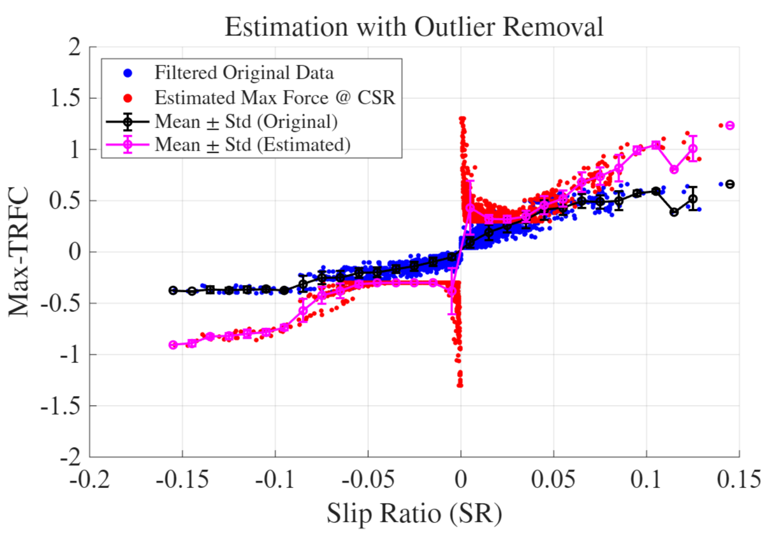

Figure 2 Illustration of Estimation Error Quantification

Using Equation (7) we establish the relationship between estimation error, CSR, and the peak TRFC. Physically, the peak TRFC can be considered equivalent to the feasible maximum acceleration. Therefore, we define $e(a_t)$ as a function that maps acceleration to the expected estimation error. This function serves as the foundation for our slip-based control algorithm design, which will be further discussed in the experimental section.

In practice, each spatial location may typically be sampled only once during the measurement process. However, by intentionally routing multiple autonomous vehicle (AV) through the same location multiple times, it is possible to obtain multiple independent observations, and the estimation error can be further minimized by aggregating multiple independent observations. The routing method will later be discussed section 4.

2.5. High slip ratio controller design

As illustrated in Figure 3,we investigate a scenario where the ego AV drives in a car-following model interacting with a preceding human vehicle and a following vehicle.

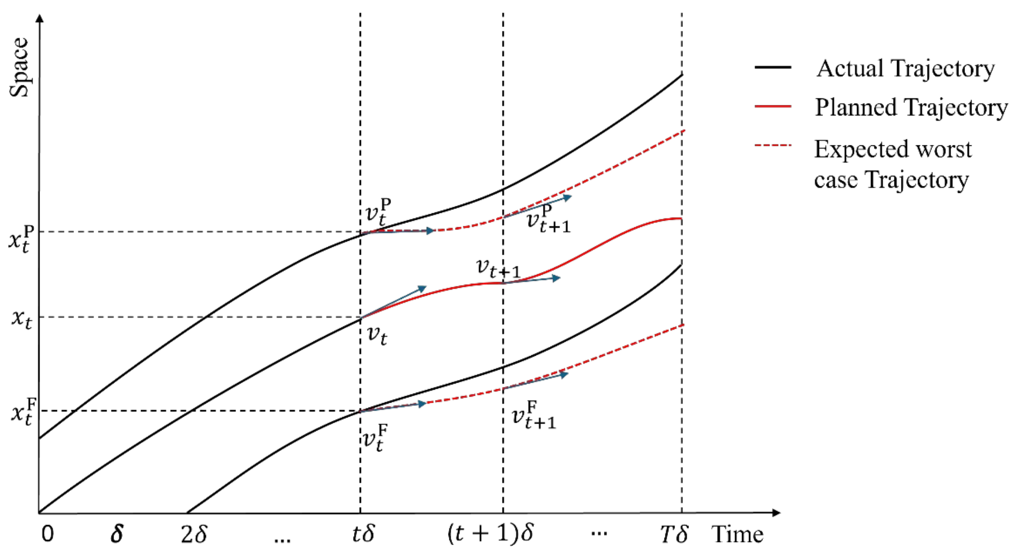

Figure 3 Illustration of Controller Status

Consider a set of discrete time indexes $T=\{0,1,2,\ldots,T\}$. Define x_t, v_t, and a_t as the location, velocity, and acceleration of the ego AV at time δt with a unit time interval $\delta, \forall t \in T$. Similarly, define $x_t^P, x_t^F, v_t^P, v_t^F, \wedge a_t^P, a_t^F$ as the position, velocity, and acceleration of the preceding vehicle and following vehicle at time δt, respectively. Where the supperscript P and F refer to the preceding and following vehicles. Let $\lambda > 0$ be a regularization weight rewards control oscillations.

To ensure the safety of the AV and surrounding vehicles during high slip ratio control, a worst-case safety assumption is adopted. Specifically, it is assumed that the preceding vehicle performs maximum deceleration while the induced acceleration of the following vehicle remains in the safety region. Under these conditions, the AV's planned motion must guarantee that no collision occurs.

The assumptions are as follows:

- Preceding vehicle maximum deceleration $-b$.
- Following vehicle follows an IDM model bounded by maximum allowed deceleration a.
- Ego AV's acceleration: $a_{min} \leq a_t \leq a_{max}$.
- The following optimization is only solved at time step where: $\$ v_t > v_{threshold} = 2 m/s$.

The high slip ratio controller can then be formulated as the following optimization problem:

$$Min \sum_{t \in T} \left[e(a_t) - \lambda \cdot (a_t - a_{t-1})^2 \right] \quad \text{s.t.}$$

$$
\begin{aligned}
& v_{t+1}^P = max\{v_t^P - b\delta, 0\}, \forall t \in T \text{¿} \{T \text{¿}\} \\
& x_{t+1}^P = x_t^P + (v_t^P + v_{t+1}^P) \cdot \frac{\delta}{2}, \forall t \in T \text{¿} T\} \\
& v_{t+1} = max\{v_t + a_t \cdot \delta, 0\}, \forall t \in T \text{¿} T\} \\
& x_{t+1} = x_t + v_t \cdot \delta + \frac{1}{2} a_t \cdot \delta^2, \forall t \in T \text{¿} T\} \\
& a_{min} \leq a_t \leq a_{max}, \forall t \in T \\
& a_t^F = a_{IDM}(v_t^F, x_t^F, v_t, x_t) \leq a, \forall t \in T \\
& v_{t+1}^F = max\{v_t^F - a\delta, 0\}, \forall t \in T \text{¿} \{T \text{¿}\} \\
& x_{t+1}^F = x_t^F + (v_t^F + v_{t+1}^F) \cdot \frac{\delta}{2}, \forall t \in T \text{¿} T\} \qquad x_t^P > x_t > x_t^F, \forall t \in T
\end{aligned}
\tag{8}
$$

3. Controller experiment

To validate the effectiveness of the proposed high-slip-ratio control and TRFC estimation framework, we conduct experiments in both simulation and real-world settings. The objective is to assess whether the framework can (i) reliably excite the high-slip regime under realistic car-following constraints, (ii) accurately estimate the peak TRFC using projection-based statistical methods, and (iii) maintain safety and control feasibility throughout the maneuver.

3.1. Initial calibration of $e(a_t)$

For operational deployment, an initial calibration of the function $e(a_t)$ is required for the OCP controller. During real-time operation, $e(a_t)$ can be updated as needed to reflect current road conditions. In the calibration phase, the AV is manually driven using intentionally exaggerated driving maneuvers to induce higher slip ratios, enabling the estimation of friction characteristics under more extreme conditions.

Once sufficient sample data is collected, we apply the prediction and error evaluation procedure described in Section . As shown in Figure 4, the relationship between acceleration a_t and the corresponding squared error can be effectively modeled using a Gaussian distribution, with a root mean squared error (RMSE) of 0.0303.

It is also noteworthy that the fitted Gaussian curve is not symmetric with respect to a_t, suggesting a possible asymmetry in the tire characteristics of the test vehicle between acceleration and deceleration phases. This imbalance may reflect differences in traction performance or drivetrain dynamics that influence the observed error profile.

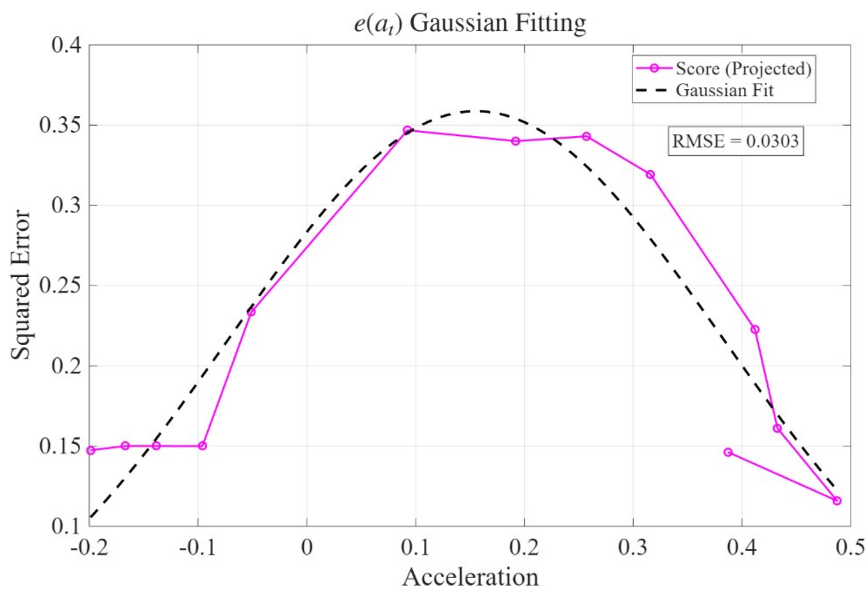

Figure 4 $e(a_t)$ *Gaussian Fitting*

3.2. Simulation setup

We implement the proposed high-slip-ratio controller and projection-based TRFC estimator in a closed-loop simulation environment developed in MATLAB/Simulink. The ego vehicle follows a preceding vehicle that applies maximum deceleration to emulate a worst-case car-following scenario. The control strategy is based on the optimal control formulation described in Section 2.5, with the acceleration-error function $e(a_t)$ calibrated as described in Section 3.1. The simulation integrates realistic longitudinal dynamics, including slope-induced gravitational force, aerodynamic drag, and dynamic load transfer between front and rear axles. The control loop is executed at 10 Hz. The ego vehicle starts from an initial speed of 10 m/s and maintains a headway of 10 meters. Safety constraints are enforced throughout the simulation to ensure no collisions occur with either the preceding or following vehicle during high-slip excitation.

3.3. Simulation result and analysis

The simulation results presented in Figure 5 demonstrate the effectiveness of the proposed high-slip-ratio control framework in safely exciting the critical region of the tire-road friction curve. This excitation is sufficient to expose the peak TRFC, which is essential for reliable friction estimation.

In the worst-case scenario where the preceding vehicle applies maximum deceleration, the ego vehicle successfully maintains safe longitudinal spacing from both the preceding and following vehicles. As shown in the position and velocity plots, all three vehicles exhibit smooth and stable trajectories, with the ego vehicle responding appropriately to the deceleration event without compromising safety. The acceleration profile of the ego vehicle shows initial oscillations during the slip excitation phase but quickly stabilizes within safe bounds. This controlled behavior indicates that the proposed controller effectively balances slip-ratio excitation with inter-vehicle safety constraints. The following vehicle also maintains sufficient headway, confirming that the overall system remains stable throughout the maneuver.

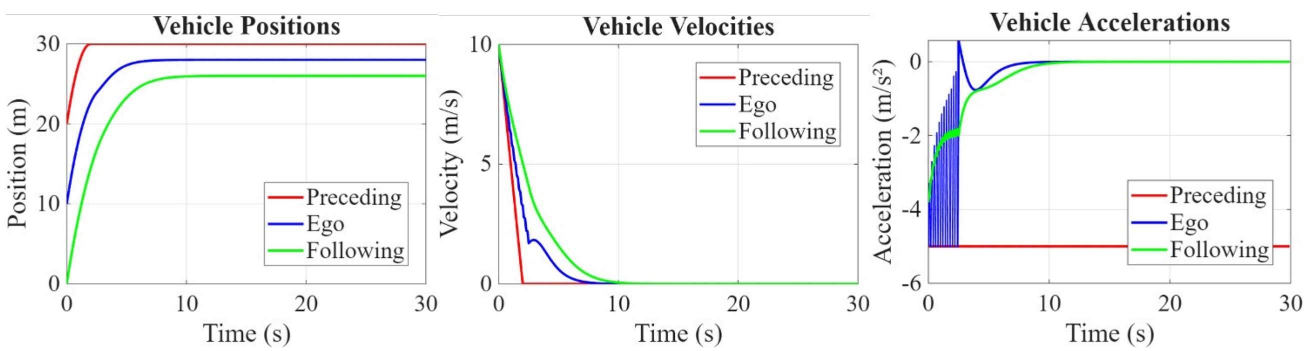

Figure 5 Simulation of Controller in Worst-case Scenarios

These results validate a core contribution of this work: accurate and scalable TRFC estimation can be achieved through deliberate slip excitation using automated vehicles operating in realistic car-following scenarios. Importantly, the approach does not rely on any dedicated friction-sensing hardware, enabling practical deployment in real-world AV systems.

3.4. Real-world validation

To evaluate the performance of the proposed friction estimation method under realistic operational conditions, we conducted a series of field experiments using our autonomous vehicle (AV) testbed at the University of Wisconsin-Madison (Figure 6). The AV platform is equipped with a high-resolution LiDAR, a GPS/INS unit for precise localization, and a control-by-wire interface that enables direct actuation of throttle, brake, and steering systems. The vehicle also supports real-time data logging and closed-loop execution of planned trajectories and acceleration profiles, making it well-suited for tasks involving longitudinal slip excitation and TRFC estimation.

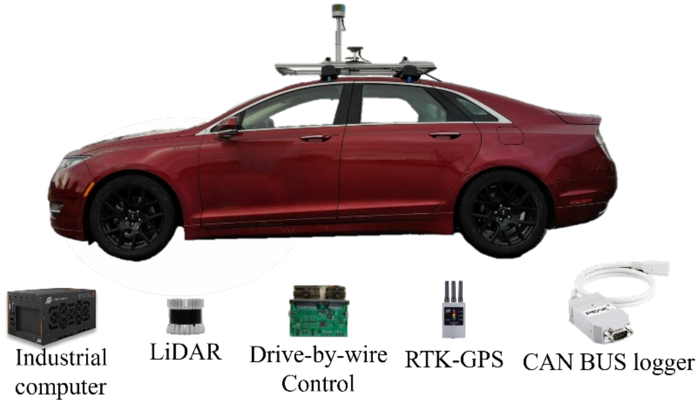

Figure 6 Field Testing Platform

The field tests were conducted along a designated stretch of Sub-Zero Parkway in Fitchburg, Wisconsin, under dry concrete surface conditions (Figure 7(a)). During each test, the AV executed a controlled sequence of acceleration and deceleration maneuvers, following a virtual lead vehicle trajectory while adhering to safety constraints defined by a car-following policy. This ensured repeatable slip generation while preserving safe longitudinal gaps.

TRFC values were estimated offline from the recorded sensor data using the proposed Simplified Magic Formula-based estimator. To improve robustness and mitigate local estimation noise, each test scenario was repeated multiple times.

As illustrated in Figure 7(b), the proposed estimation method produced consistent and spatially coherent TRFC projections across multiple independent test runs. The observed repeatability highlights the method's robustness to environmental variability and sensor noise, supporting its potential for real-world friction mapping applications. It is important to note, however, that the reliability of the projection is inherently influenced by the vehicle's executed maneuvers-smaller acceleration or deceleration inputs can result in increased estimation variance due to insufficient slip excitation. While the current setup, involving a single AV performing repeated test runs, provides a useful baseline for validating the projection approach, the methodology could be further enhanced by deploying a fleet of AVs executing this algorithm during routine empty-haul operations. Such a deployment would enable broader spatial coverage and statistical reinforcement of localized friction estimates.

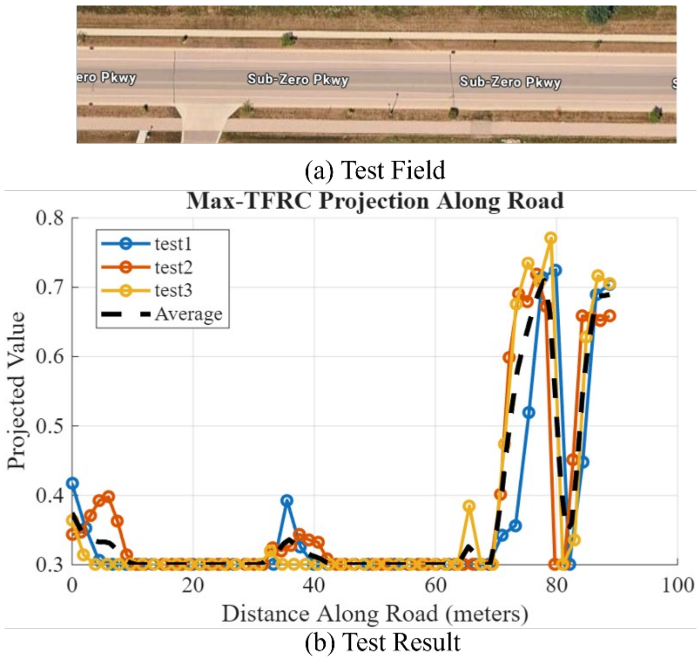

Figure 7 Field testing location and result

4. Network operation

We now analyze how to use data from vehicle sensors to obtain estimates of the Max-TRFC of a set of roadway segments $r=1,\ldots,R$ in a network. Each roadway segment is assumed homogeneous inside. A vehicle, indexed by n, belongs to a set N_r as long as it makes $Z_{n,r}>0$ measurements of slip ratio and TRFC, $\{\kappa_{n,r,z},\mu_{n,r,z}\}_{z=1}^{Z_{n,r}}$, on roadway segment r. The vehicle is equipped with connected sensors inside the tires (as those used to activate ABS) to measure angular wheel speeds. The measured value of $\kappa_{n,r,z}$ is based on the difference between the vehicle's actual travel speed (estimated from GPS data) and the speed estimated from the angular rotation of the wheels. The value of $\mu_{n,r,z}$ is derived approximately from the vehicle's acceleration records from the vehicle's accelerometer using the four-wheel vehicle model, thus accounting for weight, aerodynamic resistance, yaw, pitch and rotation [25]

Two groups of vehicles will be used. The first group consists of regular vehicles (RVs), which are operated by independent drivers who have their exogenous travel activities, routes and acceleration/deceleration patterns. However, any data collected by their sensors is shared in real-time. These vehicles are expected to experience only mild tire excitation levels, except in emergency situations that require sudden acceleration or hard braking. As a result, they will mainly provide measurements of $\kappa_{n,r,z}$and $\mu_{n,r,z}$ values that are typically far from the peak of the MF curve; e.g., either in the free rolling regime, or, in the rare event where the driver performs a hard brake, in the full skid regime, as illustrated in Figure 8(b). The second group comprises a fleet of autonomous vehicles (AVs), whose routes and acceleration/deceleration activities are remotely controlled by the transportation agencies. They can be potentially used as inspection vehicles while not carrying passengers. The agencies can control both the routes these vehicles take (to cover the entire roadway network) and their acceleration/deceleration profiles (to obtain friction measurements at higher tire excitation levels near the peak of the MF curve).

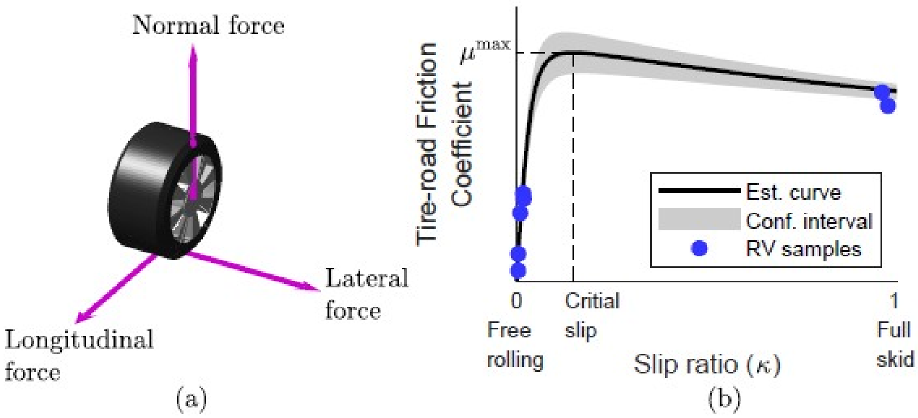

Figure 8 Tire-road friction: (a) typical forces; (b) slip vs. friction relationship.

4.1. Individual vehicle on a segment

We recognize that the friction between the roadway surface and the vehicle type depends not only on the roadway surface properties, but also on the vehicle and tire characteristics such that as the wheel radius, the tire type and condition (e.g., air pressure, rubber quality), etc. Also, each vehicle may be subject to systematic bias and precision issues. Therefore, we must first develop individual MF curve for each vehicle-segment combination.

The set of measurements $\left\{ \left(\kappa_{n,r,z}, \mu_{n,r,z} \right) \right\}_{z=1}^{Z_{n,r}}$ from vehicle n on roadway segment r will be used to estimate the semi-empirical parametric MF (5) from nonlinear least square regression[1]. The model parameters are estimated as follows:

$$\begin{aligned}
\left(\hat{\mu}_{n,r}^{max}, \hat{\beta}_{1,n,r}, \hat{\beta}_{2,n,r}, \hat{\beta}_{3,n,r} \right) &= arg \min_{\mu_{n,r}^{max}, \beta_{1,n,r}, \beta_{2,n,r}, \beta_{3,n,r}} S\left(\mu_{n,r}^{max}, \beta_{1,n,r}, \beta_{2,n,r}, \beta_{3,n,r} \right) \\
&= arg \min_{\mu_{n,r}^{max}, \beta_{1,n,r}, \beta_{2,n,r}, \beta_{3,n,r}} \sum_{z=1}^{Z_{n,r}} \left[\mu_{n,r,z} - \mu\left(\kappa_{n,r,z} \middle| \mu_{n,r}^{max}, \beta_{1,n,r}, \beta_{2,n,r}, \beta_{3,n,r} \right) \right]^2,
\end{aligned} \tag{9}$$

where $S\left(\mu_{n,r}^{max}, \beta_{1,n,r}, \beta_{2,n,r}, \beta_{3,n,r} \right)$ is the sum of squared errors. The minimization problem can be solved by most gradient-based methods such as steepest descent or Gauss-Newton algorithms.

We assess the confidence and the dispersion around these estimates using an asymptotic approximation [26]. Assuming that Equation (5) is subject to an i.i.d. Gaussian error with mean zero and equal variance, the

[1] A more conventional approach would be to use maximum likelihood estimation. We choose nonlinear least squares purely for simplicity

Jacobian matrix $J_{n,r}$ and the variance-covariance matrix $\Sigma_{n,r}$ for the estimated parameters, evaluated at the sampled points, are:

$$J_{n,r} = \left[\frac{\partial \mu \left(\kappa_{n,r,z} \middle| \left(\hat{\mu}_{n,r}^{max}, \hat{\beta}_{1,n,r}, \hat{\beta}_{2,n,r}, \hat{\beta}_{3,n,r} \right) \right)}{\partial \left(\hat{\mu}_{n,r}^{max}, \hat{\beta}_{1,n,r}, \hat{\beta}_{2,n,r}, \hat{\beta}_{3,n,r} \right)} \right]^T, \tag{10}$$

$$\Sigma_{n,r} = \frac{S\left(\mu_{n,r}^{max}, \beta_{1,n,r}, \beta_{2,n,r}, \beta_{3,n,r} \right)}{Z_{n,r} - 4} \left(J_{n,r}^T J_{n,r} \right)^{-1} \tag{11}$$

The diagonal of $\Sigma_{n,r}$ contains the variances of each of the estimated parameters. We use $\sigma_{n,r}^2$ to denote the first diagonal entry in $\Sigma_{n,r}$ that corresponds to the estimator $\mu_{n,r}^{max}$.

As mentioned before, AVs are expected to collect measurements at a wider range of slip ratios, and hence the Max-TRFC estimation from these measurements are expected to be more efficient (i.e., achieving smaller variances). The logic is that with a wider range of slip ratio measurements, it becomes more likely to have measurement pairs $\kappa_{n,r,z}, \mu_{n,r,z}$ taken near the critical slip ratio. At that point, according to the definition of the MF curve, the only parameter affecting the measurement $\mu_{n,r,z}$ is the Max-TRFC, while the other parameters $\beta_{1,n,r}, \beta_{2,n,r}, \beta_{3,n,r}$ have negligible influence. In contrast, for RVs, whose measurements are typically near free-rolling or full skid conditions, the measurements are also strongly influenced by the parameters $\beta_{1,n,r}, \beta_{2,n,r}$ (e.g., recall the definition of the slope near the origin), making it much harder to estimate each parameter precisely.

4.2. Data Fusion Across Vehicles and Segments

In this section, we present the statistical framework that compiles individual estimates $\hat{\mu}_{n,r}^{max}$ across n into an estimate of the segment-specific Max-TRFC, $E[\bar{\mu}_r^{max}]$, as a property of roadway segment r. Many methods in the literature can be used to handle such a set of panel data, but this section presents a simple sequential approach. Figure 9 illustrates the key steps as well as the propagation of uncertainties.

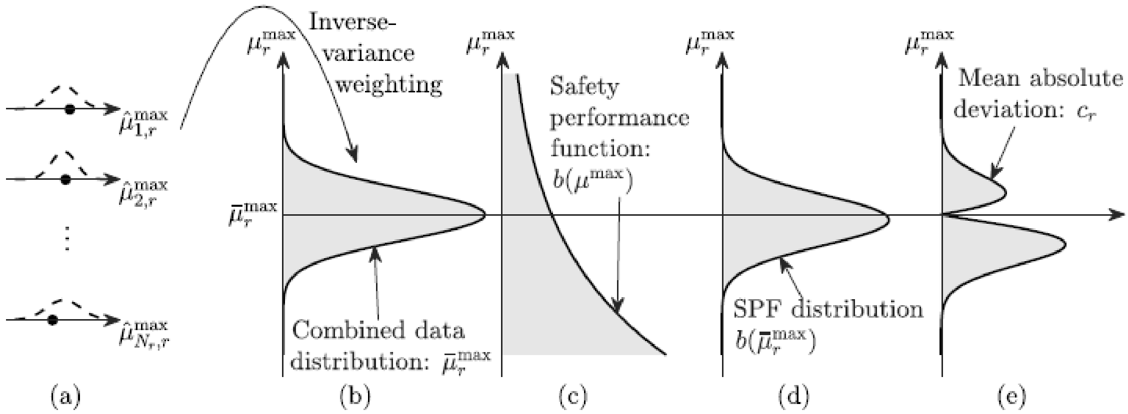

Figure 9 Illustration of the error estimation process on a roadway segment r.

First, we assume the difference in tire characteristics and conditions introduces a vehicle-specific bias Δ_n to each estimate $\hat{\mu}_r^{max}$. We already estimated the variance of $\hat{\mu}_r^{max}$ from Equation (11) as $\sigma_{n,r}^2$. Therefore, we have the following simple model:

$$\hat{\mu}_r^{max} = E\left[\bar{\mu}_r^{max}\right] + \Delta_n + \epsilon_{n,r}, \forall r = 1, \ldots, R \wedge n \in N_r, \tag{12}$$

Where we assume for simplicity that $\epsilon_{n,r}$ is an i.i.d. Gaussian error term with mean zero and variance $\sigma_{n,r}^2$; and $E\left[\bar{\mu}_r^{max}\right]$ is the expected value of the Max-TRFC estimate for arc r. Following the spirit of weighted least squares for samples with heteroskedasticity, $E\left[\bar{\mu}_r^{max}\right]$ is computed using inverse-variance weighting, giving larger weights to measurements with higher confidence (illustrated by the transition from Figure 9 (a) to (b), as follows:

$$E\left[\bar{\mu}_r^{max}\right] = \frac{\sum_{n \in N_r} \frac{\hat{\mu}_{n,r}^{max} - \hat{\Delta}_n}{\sigma_{n,r}^2}}{\sum_{n \in N_r} \frac{1}{\sigma_{n,r}^2}} \tag{13}$$

Accordingly, the first-order condition of the least-squares problem that minimizes the residuals, $\left[E\left[\bar{\mu}_r^{max}\right] - \left(\hat{\mu}_r^{max} - \Delta_n\right)\right]^2$, leads to the following system of linear equations:

$$\hat{\Delta}_n = -\hat{\mu}_{n,r}^{max} - \frac{\sigma_{n,r}^2 \sum_{z \in N_r ¿ n\}} \frac{\hat{\mu}_{z,r}^{max} - \hat{\Delta}_z}{\sigma_{z,r}^2}}{1 - \sigma_{n,r}^2 \sum_{z \in N_r} \frac{1}{\sigma_{z,r}^2}}, \forall r = 1, \ldots, R \wedge n \in N_r. \qquad (14)$$

Under our assumptions, $\overline{\mu}_r^{max}$ is a Gaussian random variable with the following variance:

$$\sigma_r^2 = \frac{\sum_{n \in N_r} \left(\frac{1}{\sigma_{n,r}^2} \right)^2 \sigma_{n,r}^2}{\left(\sum_{n \in N_r} \frac{1}{\sigma_{n,r}^2} \right)^2} = \frac{1}{\sum_{n \in N_r} \frac{1}{\sigma_{n,r}^2}}, \qquad (15)$$

which is the harmonic mean of the measurement variances from individual vehicles. Below are some simple properties of this variance.

Proposition 1. [27]*Assuming all vehicle's estimators (i.e., $\hat{\mu}_{n,r}^{max} - \Delta_n$) are unbiased, then* $min_n \{\sigma_{n,r}^2\} / |N_r| \le \sigma_r^2 \le min(min_n \{\sigma_{n,r}^2\}, max_n \{\sigma_{n,r}^2\} / |N_r|)$.

Proposition 1 demonstrates that the data from the vehicle with the highest precision (i.e., $arg\, min_n \{\sigma_{n,r}^2\}$) dominates all others, although using additional data from other vehicles always help to lower the variance. The upper and lower bounds meet when all measurements are equal; otherwise, σ_r^2 is closer to an upper bound, and one measurement will likely dominate the others. This highlights the importance of using AVs to improve measurement precision. In addition, the relative values of the two upper-bounds are crucial when we use both RVs and AVs to provide measurements. When the data come exclusively from RVs, $max_n \{\sigma_{n,r}^2\} / ¿ N_r \vee ¿¿$ is likely to provide the smaller upper bound. However, once data from an AV (typically with a much lower variance) is obtained, the first lower bound $min_n \{\sigma_{n,r}^2\}$ is likely to be tighter.

The upper and lower bounds in Proposition 1 also directly implies Corollary 1 below.

Corollary 1. *The value of σ_r converges to 0 at a rate proportional to $\frac{1}{\sqrt{¿ N_r \vee ¿¿}}$, when $¿ N_r \vee \to \infty$*

This result indicates that if the collection of $\hat{\mu}_{n,r}^{max}$ is based solely on RVs with similar $\sigma_{n,r}^2$, the convergence of $E[\overline{\mu}_r^{max}]$ is sub-linear. Therefore, Corollary 1 supports the use of AVs to collect data with lower a variance to improve the convergence rate.

4.3. Safety Implications

The motivation for accurate estimation of $E[\overline{\mu}_r^{max}]$ is to better identify problematic roadway segments, so that agencies can apply appropriate pavement treatments to improve safety. Normally, the safety impacts of accurate friction measurement are much more pronounced on roadway segments that have low Max-TRFC (e.g., icy road), because these segments often have much higher numbers of friction-related crashes.

Statistical models, called safety performance functions (SPF), have been used to reveal the expected crash frequencies caused by variations in Max-TRFC [28], [29], [30], [31]. While SPFs can be formulated in various ways, the most popular ones assume a log-linear relationship [32], as illustrated in Figure 9(c), between the expected crash rate per centerline mile and the pavement Max-TRFC on segment r, $b_r\left(E\left[\overline{\mu}_r^{max}\right]\right)$, is:

$$b_r\left(E[\overline{\mu}_r^{max}]\right)=\alpha_{1,r}\exp\left(-\alpha_{2,r}E[\overline{\mu}_r^{max}]\right),\forall r=1,\ldots,R \qquad (16)$$

where parameter $\alpha_{1,r}>0$ is a roadway specific function that captures all its roadway design and traffic operation features (e.g., segment length, number of lanes, presence of median and shoulder, AADT), and $\alpha_{2,r}\geq 0$ dictates that a larger Max-TRFC tends to result in fewer crashes.

Since $\overline{\mu}_r^{max}$ is a random variable, so is the estimated crash rate $b_r\left(\overline{\mu}_r^{max}\right)$. Given the exponential form of Equation (16), the variable $b_r\left(\overline{\mu}_r^{max}\right)$ follows a log-normal distribution with parameters $\ln\alpha_{1,r}-\alpha_{2,r}E[\overline{\mu}_r^{max}]$, and $\alpha_{2,r}^2\sigma_r^2$, as illustrated in Figure 9(d). Benefits from precise and accurate Max-TRFC estimation are ultimately measured by the mean absolute deviation (MAD) of $b_r\left(\overline{\mu}_r^{max}\right)$, as in Figure 9(e). It can be approximated by that of a regular Gaussian when the coefficient of variation is small (usually lower than 0.2, see [33]). In our context, when $\alpha_{2,r}\sigma_r<\sqrt{\ln 1.04}$, we can estimate the MAD as follows:[33]

$$c_r\overset{def}{=}MAD\left[b_r\left(\overline{\mu}_r^{max}\right)\right]\approx\left[\left(\exp\left(\alpha_{2,r}^2\sigma_r^2\right)-1\right)\exp\left(2\left(\ln\alpha_{1,r}-\alpha_{2,r}E\left[\overline{\mu}_r^{max}\right]\right)+\alpha_{2,r}^2\sigma_r^2\right)\frac{2}{\pi}\right]^{\frac{1}{2}}. \qquad (17)$$

Figure 9(e) qualitatively illustrates how MAD is not symmetrical around $E[\overline{\mu}_r^{max}]$ - everything else being equal, the value of c_r is much more pronounced for roadway segments with a lower Max-TRFC. This exactly captures the larger safety impacts of inaccurate friction measurement on roadways that have a higher tendency towards friction-related crashes.

5. Dynamic AV Routing

Now we explicitly consider the topology of the roadway network and represent it by a directed graph $G(V,E)$, where V is the set of vertices and E is the set of all arcs, including the set of Rsegments of interest. We have a fleet of L heterogeneous AVs. Sets V_i and V_i' include the in- and out-neighbors of vertex i, respectively, and $i_l \in V$ indicates the current position of an AV $l=1,\ldots,L$. We define the arcs to have approximately the same traverse time - a long roadway stretch (e.g., between consecutive entrance/exit ramps or intersections) may be subdivided into multiple segments - and they are long enough to allow AVs to accelerate/decelerate a few times to achieve proper tire excitation. For model convenience, we redefine the safety impact metric $c_{ij} \equiv c_r$ if arc $r=(i,j)$. All other additional notation for the routing problem is summarized in Appendix-II Table of Mathematical Notation Used in The AV Routing

We also divide time into equal time epochs, indexed by t, with sufficient interval duration to allow an AV to traverse and perform measurements on one arc. Routing and measurement decisions for all L AVs are made in a rolling horizon framework. Whenever a decision is made, we set the current time to be $t=0$ and look into a planning horizon of T future time intervals, $[0,T)$. Input data include the current locations of the AVs $\{i_l\}_{\forall l}$, and the latest safety benefit metrics from pavement friction measurements on all roadway segments $\{c_{ij}\}_{\forall(i,j)}$. The decision variables are

$$x_{l,ij,t}=\begin{cases} 1, \text{if } AV\ l\ measures\ arc\ (i,j) \in the\ interval\ [t,t+1) \\ 0, otherwise \end{cases} \qquad (18)$$

The vector containing all values of $x_{l,i,j,t}$ is x¿$\left[x_{l,ij,t}\right]$. Additionally, an auxiliary variable y_{ij} tracks whether any AVs will perform new measurements on an arc (i,j) at any point of the planning horizon:

$$y_{ij}=\begin{cases} 1, if\ any\ AV\ measures\ arc\ (i,j) \in the\ horizon\ [0,T) \\ 0, otherwise \end{cases} \qquad (19)$$

The vector containing all values of y_{ij} is y=$[y_{ij}]$.

Proposition 1 and Corollary 1 in the previous section suggest that repeated AV measurements on the same arc ($i,j)$ yields diminishing marginal benefits. To maximize productivity of limited AV resources, we route these controlled AVs to cover the most critical arcs (those with higher values of c_{ij} at the beginning of horizon). The problem can be formulated into the following integer program:

$$
\begin{aligned}
& \min \sum_{(i,j)\in E} c_{ij}\left(1-y_{ij}\right) \\
& s.t. \sum_{(i,j)\in E} x_{l,i,j,t}=1\,\forall l=1,\ldots,L \wedge t=1,\ldots,T-1 \\
& \sum_{j\in V_{i_l}} x_{l,i_l,j,0}=1\,\forall l=1,\ldots,L \\
& \sum_{j\in V_k} x_{l,kj,t}=\sum_{i\in V_k'} x_{l,ik,j,t-1}\,\forall l=1,\ldots,L\wedge t=1,\ldots,T-1 \\
& \sum_{l=1}^{L}\sum_{t=0}^{T-1} x_{l,ij,t}\geq y_{ij}\,\forall(i,j)\in E \\
& x_{l,ij,t}\in\{0,1\}\,\forall l=1,\ldots,L,\wedge(i,j)\in E,\wedge t=0,\ldots,T \\
& y_{ij}\in\{0,1\}\,\forall(i,j)\in E
\end{aligned}
\tag{20}
$$

Here the first set of constraints limit AV routing to one arc per AV per time step. The second set of constraints set the starting positions for the AVs. Vehicle conservation is guaranteed by the third set of constraints. The fourth set of constraints define the auxiliary variable y_{ij} based on the measurement plan within the planning horizon. The two sets of constraints define the binary decision variables.

With the rolling horizon approach, once the optimization problem (18)Error: Reference source not found is solved, only the routing and measurement decisions for the first time interval will be implemented. Then, we update $\{c_{ij}\}$ to include new AV and RV measurements, reset the current decision epoch to $t=0$, and solve (18) again for the next T time steps.

5.1. Branch-and-Price algorithm

Problem (18)Error: Reference source not found is NP-hard, but its constraints form a block structure. Each block corresponds to the routing decision of one AV. For each l, we define the feasibility region formed by these constraints, which is clearly convex, as X_l. Since each variable $x_{l,ij,t}$ is bounded as binary, X_l does not have extreme rays, and it can be re-written through its extreme points as follows:

$$X_l=\left\{x_l=\sum_{q\in Q_l}\lambda_{l,q}\bar{x}_{l,q}\,\middle|\,\sum_{q\in Q_l}\lambda_{l,q}=1,\lambda_{l,q}\geq 0\right\},\forall l=1,\ldots,L \tag{21}$$

Where Q_l is the set of all extreme points (or columns); $\bar{x}_{l,q}$ is the q-th extreme point in Q_l and $\bar{x}_{l,q}=\left[\bar{x}_{l,ij,t,q}\right]$; $\lambda_{l,q}$ is the corresponding weight or dual. Constraints $\sum_{q\in Q_l}\lambda_{l,q}=1$ and $\lambda_{l,q}\geq 0$ ensure the convexity; and x_l is the resulting route for AV l.

We apply a column generation algorithm [34] to solve the problem. Suppose that we only know a subset of the columns $\widetilde{Q}_l \subset Q_l$. We solve the following Linearly Relaxed Restricted Master Problem (LRRMP) based on these columns and linear relaxation of the variables y_{ij}:

$$\begin{aligned}
&\underset{\lambda, y}{Min} \sum_{(i,j)\in E} c_{ij}(1-y_{ij}) \\
&s.t.\ y_{ij} - \sum_{l=1}^{L} \sum_{q\in \widetilde{Q}_l} \lambda_{l,q} \sum_{t=0}^{T-1} \overline{x}_{l,ij,t,q} \le 0, \forall (i,j)\in E \\
&\sum_{q\in \widetilde{Q}_l} \lambda_{l,q} = 1, \forall l = 1,\ldots,L \\
&\lambda_{l,q} \ge 0, \forall l = 1,\ldots,L \wedge q \in \widetilde{Q}_l \\
&0 \le y_{ij} \le 1, \forall (i,j) \in E.
\end{aligned} \tag{22}$$

In addition, a set of subproblems must be solved to verify the optimality of the solutions. The subproblems are defined for individual AVs, and each uses the dual variables $\{\overline{p}_{ij}\}$ and $\{\overline{v}_l\}$ of the first and second set of constraints in (20)Error: Reference source not found, respectively, as follows:

$$\begin{aligned}
&\zeta_l = Min_x \sum_{(i,j)\in E} \overline{p}_{ij} \sum_{t=0}^{T-1} x_{l,ij,t} - \overline{v}_l \\
&s.t.\ \sum_{(i,j)\in E} x_{l,ij,t} = 1, \forall t = 1,\ldots,T-1 \qquad \sum_{j\in V_{i_l}} x_{l,i_l j,0} = 1 \\
&\sum_{j\in V_k} x_{l,kj,t} - \sum_{j\in V_k'} x_{l,ik,t-1} = 0, \forall t = 1,\ldots,T-1 \\
&x_{l,ij,t} \in \{0,1\} \forall (i,j) \in E \wedge t = 0,\ldots,T-1
\end{aligned} \tag{23}$$

The optimal objective value of ζ_l gives the minimum reduced cost among all extreme points, including those that are not currently used in the LRRMP. The corresponding solution, $\overline{x}_{l,q} = [\overline{x}_{l,ij,t,q}]$ is an extreme point of X_l. If $\zeta_l < 0$ for any $l = 1,\ldots,L$, the extreme point $\overline{x}_{l,q}$ is included in $\widetilde{Q}_l$, thus serves as a base for a new column in the LRRMP. With this new column, LRRMP is solved again. The iterative process between LRRMP and subproblems is repeated, until $\zeta_l \ge 0, \forall l = 1,\ldots,L$, indicating that the current solution of the LRRMP is optimal already.

Note that subproblem (21)Error: Reference source not found is a shortest path problem for one AV, l, and $\overline{x}_{l,q}$ describes a route in a time-space network [35]. However, this network does not contain cycles, but arc cost $\overline{p}_{ij}$ can be negative, and, hence, the standard Dijkstra algorithm is not suitable. Therefore, we use topological sorting for the lowest complexity [36]. Each AV's origin is its current position at time $t=0$, and its destination is an added dummy node at time step T. This dummy node is connected to every node in the network at the previous time step $T-1$ with null cost (see Figure 10 for an illustration).

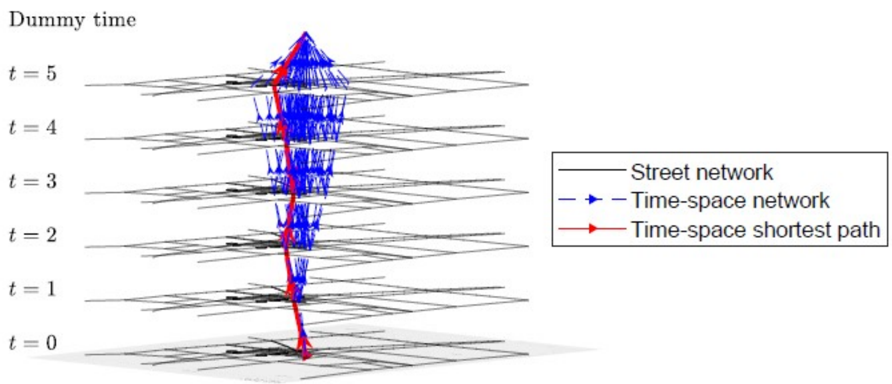

Figure 10 Illustration of The Time-space Network for a Subproblem, Where T = 6.

[34]If its solution of the column generation algorithm is not integer, we perform the branching on a variable $x_{l,i,j,t}$that is closest to 0.5 and corresponds to the smallest t, as part of a Branch-and-Price algorithm [37]. The branching is equivalent to forcing the passage of an AV l through arc (i, j) at time t (i.e., $x_{l,ij,t}=1$) or forcing its avoidance entirely (i.e., $x_{l,ij,t}=0$) in the time-space network. For the latter, we can directly remove the arc that we want the vehicle to avoid from the time-space network. For the former, to force the AV to traverse an arc, we remove all other arcs at the specific level of the time-space network. The active branching nodes in the search tree are explored through a depth-first principle.

While implementing the Branch-and-Price algorithm, instead of exploring the branched nodes sequentially, we parallelize the computation at different nodes through multi-threaded computer processors. Since the computing time at each node is unknown *a priori*, depending on the column generation convergence, we chose to implement an asynchronous parallel computing framework. This framework dedicates one of the processor's cores to be the coordinator, which continuously retrieves information from the other cores, coordinates their computation tasks, and allocates new tasks whenever a core becomes idle. Meanwhile, the other cores must handle feasibility and quality checks and solve the LRRMP (if feasibility and quality checks allow) solely at the node allocated by the coordinator. Whenever an integer solution is found, the coordinator uses this new result to halt on-going tasks at other cores that have become sub-optimal.

6. Case study

6.1. System setting

The proposed models and algorithms are implemented for the Champaign County, Illinois (about 130 miles south of Chicago), whose road network comprises a total of 800 miles in centerline length of interstate, primary, and secondary roads, as well as ramps and junctions. The network is partitioned into 652 directed segments (i.e., arcs), each taking about 2 minutes for an AV to traverse (at a speed of 30-35 mph).

The ground-truth of Max-TRFC on a simulated arc was randomly generated using a Gaussian distribution with a mean of 0.5 and a variance of 0.05, which is further censored into the realistic range [0.1, 0.9]. The assumed

SPF for every arc in the network has the form $b_r\left(E[\bar{\mu}_r^{max}]\right)=2500\cdot\exp\left(-2E[\bar{\mu}_r^{max}]\right)$ [crashes/10^8VMT].

The network is integrated into an RV traffic simulation environment. To replicate realistic traffic patterns, we utilize traffic count data from the Illinois Department of Transportation (IDOT)[2]. This dataset does not cover all arcs in the road network, so we estimate origin-destination (OD) pairs that can replicate the traffic counts available in the IDOT dataset based on [38]. For simplicity, the simulation assumes that all RVs travel along the shortest-time path. The simulation also assumes that RVs travel at the speed limit of each arc, which may be faster than the controlled AVs (which travel at 30-35 mph).

Figure 11(a) illustrates the original road network and the positions of traffic sensors used to estimate RV traffic patterns. Figure 11(b) depicts the abstracted network with the respective arc traffic volumes. The estimated traffic counts (derived from the generated OD pattern) fit with the IDOT data with an $R^2=0.95$.

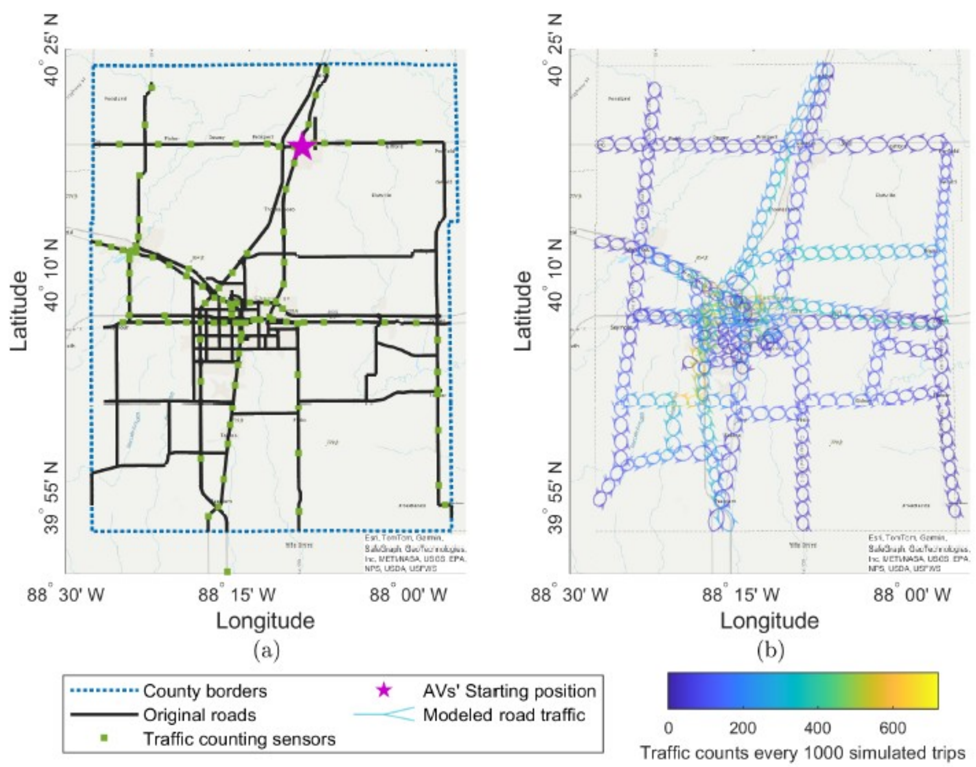

Figure 11 Champaign County case study: (a) roadway network and traffic sensors; (b) network abstraction with simulated traffic.

6.2. Computational result

The models, algorithms, and the simulation environment are implemented in MATLAB R2024a on a computer with an Intel Core i7-14700 at 2.10 GHz processor with 32 GB of RAM at 4400 MT/s and a 64-bit Windows 11 Enterprise operating system. The LRRMP model is solved by HiGHS, a high-performance serial and parallel software for solving large-scale sparse linear programming, mixed-integer programming, and quadratic programming models [39]. Each simulation was repeated 20 times for consistency.

[2] Transportation Data Management System, accessible at: idot.ms2soft.com/tcds/.

Traffic is simulated for a total of 3 hours (after 30 minutes of warm-up period). The base scenarios consider a fleet size $L=2$ AVs and a planning horizon with $T=5$ time steps unless otherwise noted. Each time step is 2 minutes in duration, thus each round in the rolling horizon framework plans the next 10 minutes of AV measurements. In this period, about 100 RVs start their trips every hour, providing their Max-TRFC estimates over time.

6.3. Base scenario

In our initial analysis, we focused on demonstrating the potential of cooperation between the RVs and AVs in collecting Max-TRFCs. For this cooperation to be effective, the measurement data need to be fused, and the biases of the RVs and the AVs must be estimated. In our experiment, the panel data that are used for fitting Equation (12) come from the 2 AVs and 98.4% of all 354 RVs per simulation. The remaining 1.6% of RVs only make measurements on arcs that no other vehicle traversed during the 3 hours of simulation.

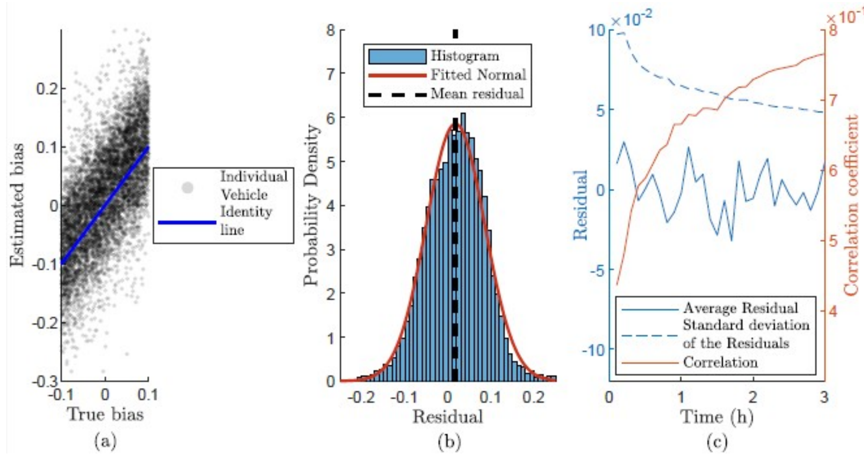

Figure 12 Estimation bias LSQ

Figure 12(a) shows a strong correlation between the true bias and the estimated bias among all AVs and 98.4% of RVs. Figure 12(b) plots the histogram of residuals, which very well fits into a normal distribution with a zero mean. Figure 12(c) highlights how, as more friction data are compiled and corrected over time, the average of the residuals fluctuates near zero, the standard deviation of the residuals gradually decreases, and the correlation coefficient between the estimated biases and the true biases increases.

Once biases have been estimated, we compile Max-TRFCs and measure how errors in Max-TRFC estimates affect safety performance predictions when compared to a 'do-nothing' scenario (i.e., no measurements are taken by any RVs or AVs) over time. The results are shown in Figure 13(a).

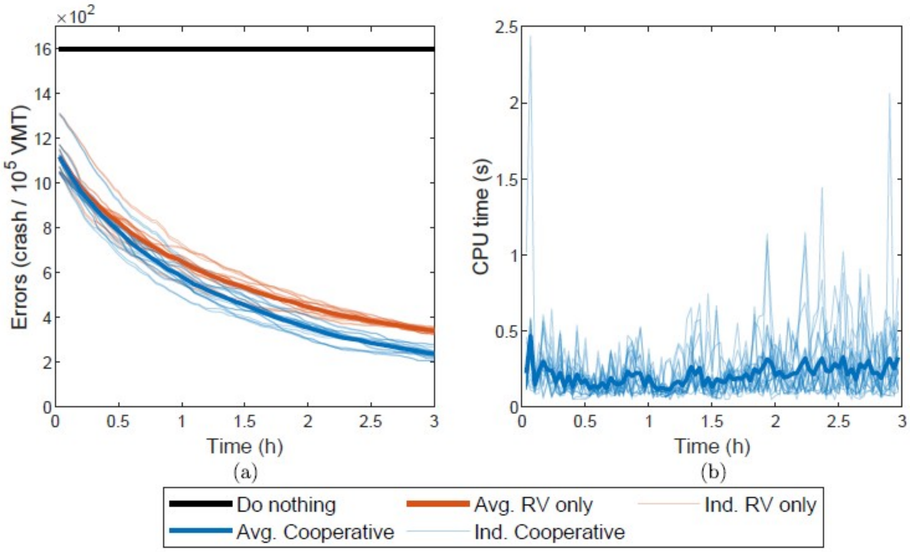

Figure 13 Base scenario: (a) reduction in crash estimate errors; (b) computational times to solve AV routing in each rolling horizon.

The 'RV only' cases show that even RVs alone can provide valuable initial information about the network within a few hours. However, they struggle to deliver a more accurate depiction of pavement conditions due to the sub-linear decrease in the MAD when making their measurements alone. Each instance ('Ind. RV only') shows some scatters over time as compared to the average ('Avg. RV only'). For example, during the first 30 minutes, errors dropped from 1190 to 830 crashes/10^8VMT (30% reduction) as 370 measurements taken during this period. It takes an additional 54 minutes to drop errors another 360 crashes/10^8VMT after 1125 new measurements are taken during this period.

Figure 13(a) also demonstrates how routing of AVs improves the sub-linear MAD convergence from RVs. Even with just a couple of AVs departing from a single location (shown in Figure 11(a)), the 'Cooperative' cases show notable improved error reduction and smaller scatters between the individual instances ('Ind. Cooperative') and the average ('Avg. Cooperative'). In this scenario, errors reach the same 30% reduction 15 minutes earlier with 300 fewer measurements than that needed in the 'RV only' cases. And, a 35% lower error is achieved at the end of the 3-hour time horizon.[3]

Figure 13(b) shows that most computation time for the routing problem at each decision epoch ranges from 0.05-0.5 seconds for all instances (marked by the 'Ind. Cooperative' entries), and that the average ranges between 0.1-0.3 seconds (marked by the 'Avg. Cooperative'), which is far less than the 2-minute duration needed for rolling horizon implementation.

It is also insightful to take a closer look at how the AV routes evolve within the rolling horizon framework. Figure 14(a) and (b) depict the planned paths of one AV at time steps 1 and 2, respectively. The solution at time step 1 says that the AV was to make a U-turn at the end of time step 3; however, this action was postponed by the decision at time step 2, and the AV continues to move eastbound for one more time step. This decision

[3] After a certain subset of arcs have been measured, improvement of network-wide friction measurements slows down, because AVs may have to increasingly deadhead across less important but "convenient" arcs. Future research could systematically seek a balance between overall friction measurement coverage and deadheading of the AVs.

shows that the routing problem identified that measuring a couple more arcs to the east would yield lower errors than any arcs to the west over the next 10 minutes. Figure 14(c) and (d) display the entire paths for both AVs. AV routes are concentrated in rural areas, outside the urban area of Champaign-Urbana. These rural areas, with fewer RV trips, received fewer RV measurements and exhibited higher friction uncertainty.

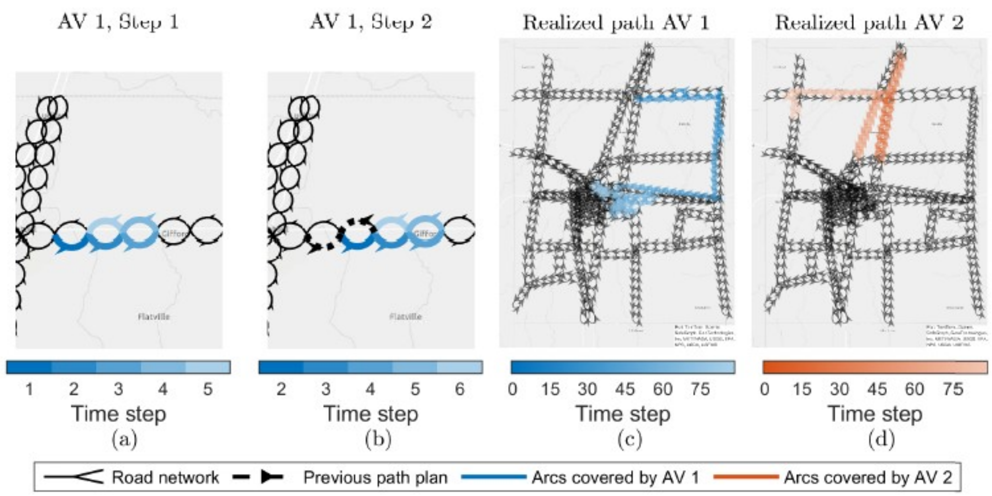

Figure 14 Base scenario: (a) planned path for AV 1 at step 1; (b) updated path plan for AV 1 at step 2; (c) complete path of AV 1 during the simulated period; (d) complete path of AV 2 during the simulated period.

We can also observe the sub-linear convergence of MAD as RV measurements accumulate in an arc on Interstate 74 (between Neil St. and Lincoln Ave.), north of Urbana. In Figure 15(a), the error estimate steadily decreases with each RV measurement. However, convergence remains sub-linear: the errors barely change after 10 RV measurements, not until the arc receives a measurement from an AV (the 19th measurement). That AV estimate reduces MAD error estimate from around 25 to approximately 6 crashes/10^8VMT. Figure 15(b) shows RVs initially overestimating the Max-TRFC during the first few measurements. Eventually, the Max-TRFC estimate converges to the true Max-TRFC value, and the introduction of an AV measurement further narrows the confidence interval.

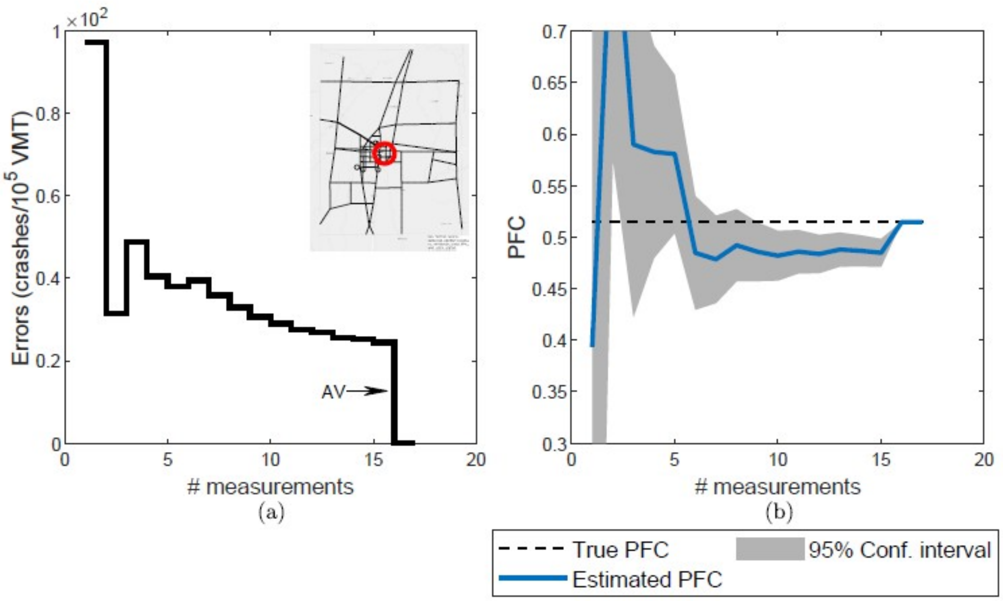

Figure 15 Evolution of Estimates for a Single Arc on Lincoln Ave.: (a) Crash MAD; (b) Max-TRFC.

6.4. Sensitivity analysis

We assess the impact of varying the number of RVs that are making measurements per unit time. Figure 16 shows how an average arc's crash MAD changes as the number of hourly RV trips increases from 50 to 500. It clearly shows diminishing marginal returns: further halving the errors requires roughly three to four times more RV trips. The box plots also show that the interquartile ranges become narrower with larger numbers of hourly RV trips, indicating that estimate errors $\{c_{ij}\}$ become more homogeneous across all arcs in the network.

Figure 17 illustrates how three key performance indicators of the routing problem varied with fleet size L and number of time intervals in the planning horizon T. Figure 17(a) shows that average crash MAD decreases with both larger fleets and longer planning horizons. However, beyond $T>3$ time intervals, most improvements result from increasing L. Figure 17(b) presents the number of arcs that are covered by the AVs at least once. This metric is closely aligned with that in Figure 17(a): for $T>3$, larger fleets enable AVs to cover more of the network, thereby reducing estimation errors. Figure 17(c) reports the average computational time per decision epoch for solving the AV routing problem. As expected, time grew exponentially with both L and T, as indicated by the spacing of the isoquant curves. Nonetheless, average times stayed under the 2-minute threshold, except for 19% of instances with $L=5$ and $T=10$ (average CPU time of 108 seconds). This implies that real-world applications of the model may have a small optimality gap. These findings suggest using moderate planning horizon lengths ($T<7$ time intervals, in this case) when examining larger networks.

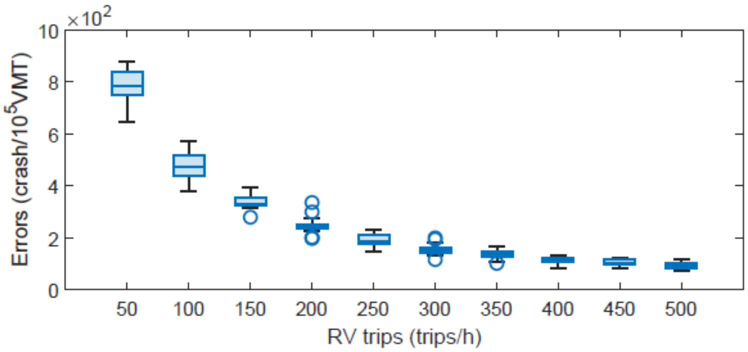

Figure 16 Average arc measurement error vs. the number of hourly RV measurements.

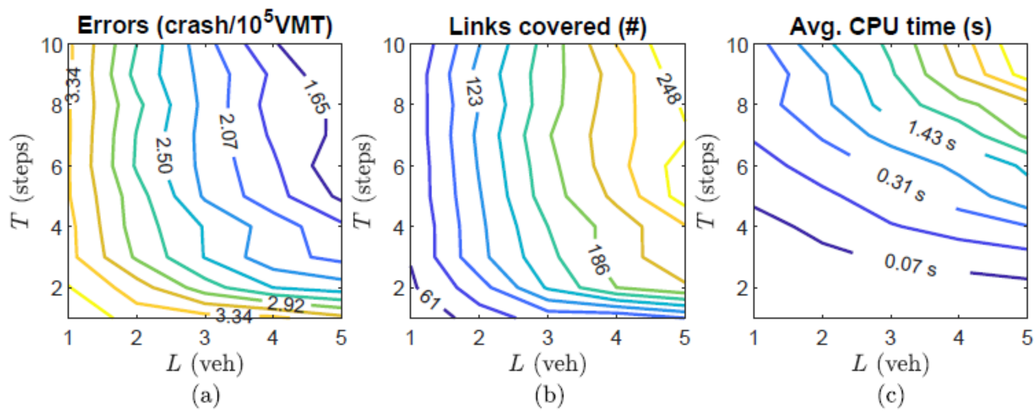

Figure 17 Sensitivity analysis: (a) average crash MAD at the end of the simulation; (b) number of segments covered by AVs at the end of the simulation; (c) average CPU time to solve routing problem at each time step.

7. Finds and conclusion

This project developed and demonstrated a comprehensive framework for dynamic pavement friction measurement that integrates both uncontrolled RV-based sensing and controlled AV-based active excitation. Measurements collected from uncontrolled RVs provide a rapid and cost-effective initial estimate of network-wide pavement conditions. However, their accuracy and spatial coverage are highly dependent on trip distribution and driving behavior, motivating the deployment of AVs with controlled acceleration maneuvers to fill measurement gaps and enhance coverage, particularly in rural or under-sampled areas.

To further improve robustness, we introduced a high-slip-ratio active control and estimation framework that leverages the flexibility of AVs during empty-haul trips. By deliberately exciting higher slip ratios under safe conditions, this approach overcomes the limitations of conventional low-excitation measurements and enables reliable estimation of peak tire-road friction. The use of a simplified Magic Formula tire model and binning-based statistical projection strengthens the accuracy of estimates in the presence of local data sparsity and sensor noise, while constrained optimization ensures trajectory tracking and inter-vehicle safety.

The proposed strategy also emphasizes the need for a structured data framework. By segmenting the road network into arcs and fusing multiple data sources, the system links vehicle geolocation with friction readings to form scalable, infrastructure-level friction maps. This enables authorities to prioritize segments with lower friction, which are more strongly associated with crash risks. Moreover, concepts from sensor fusion improve the differentiation of measurements by reliability, thus enhancing the precision of combined estimates.

While the framework demonstrates accuracy, scalability, and safety in both simulation and field validation, several limitations remain. Operational costs associated with AV deployment were not explicitly modeled, but could be incorporated through estimation-error penalties and cost functions. Environmental factors such as weather introduce additional variability, underscoring the importance of long-term testing under diverse conditions. Cooperative fleet-based sensing, including AV rentals or partnerships with ride-sourcing operators, could extend network coverage at lower cost.

Future work will focus on real-time implementation at scale, long-term deployment under varying roadway and weather conditions, and integration with broader urban infrastructure monitoring. This includes leveraging vehicle-mounted inertial sensors for pavement deformation detection, combining AV and RV data streams for continuous friction mapping, and even incorporating emerging platforms such as urban air mobility for air-quality and pollution sensing. These directions highlight the potential of coordinated RV-AV sensing systems not only for pavement management but also for advancing resilient, safe, and data-driven urban mobility.

Appendix-I Table of Mathematical Notation Used for Tire-Road Estimation

Notation	Description
μ	Tire-road friction coefficient (TRFC)
κ	Slip ratio
$\beta_{¿}$	Parameters of the MF model
μ^{max}	Maximum tire road friction coefficient (Max-TRFC/PFC)
R	Number of roadway segments
N_r	Set of vehicles who took slip ratio and TRFC measurements at arc r
$Z_{n,r}$	Number of collected slip ratio vs TRFC measurements collected by vehicle n on arc r
$\kappa_{n,r,z}$	The z-th slip ratio measurement collected by vehicle n on arc r

Notation	Description
$\mu_{n,r,z}$	The z-th TRFC measurement collected by vehicle n on arc r
$\hat{\beta}_{\text{¿},n,r}$	Estimated parameters of the MF model for vehicle n on arc$r$
$\hat{\mu}_{n,r}^{max}$	Estimated Max-TRFC from vehicle n on arc r
$J_{n,r}$	Jacocian matrix of the MF model estimated by vehicle n on arc r
$\Sigma_{n,r}$	Covariance matrix of the estimated parameters of the MF model for vehicle n on arc r
Δ_n	Bias in the estimated Max-TRFC from vehicle n
$\hat{\Delta}_n$	Estimated bias in the estimated Max-TRFC for vehicle n
$\sigma_{n,r}^2$	Variance associated with the estimated Max-TRFC from vehicle $n$on arc r
$\epsilon_{n,r}$	Error term associated with the bias for vehicle n on arc r
$\overline{\mu}_r^{max}$	Combined Max-TRFC estimate for arc r
$E[\overline{\mu}_r^{max}]$	Expected values of the combined Max-TRFC estimate for arc r
σ_r^2	Variance associated with the estimated Max-TRFC for arc r
$b_r(\cdot)$	Safety Performance Function (estimates the crash rates for a given Max-TRFC on arc r)
$\alpha_{\text{¿},r}$	Parameters of the SPF model for arc r
c_r	Mean Absolute Deviation of the estimated crash rate for arc r

CENTER FOR CONNECTED AND AUTOMATED TRANSPORTATION

UMTRI
The University of Akron
Central State University
ILLINOIS CENTER FOR TRANSPORTATION
University of Minnesota
Northwestern
PURDUE UNIVERSITY
Washtenaw Community College
WISCONSIN UNIVERSITY OF WISCONSIN–MADISON

Appendix-II Table of Mathematical Notation Used in The AV Routing

Notation	Description
E	Set of edges in the road network
V	Set of vertices in the road network
V_i	Set of out- neighbors to vertex i
V_i'	Set of in- neighbors to vertex i
i_l	Current position of AV l
c_{ij}	Mean Absolute Deviation c_r of the estimated crash rate on arc $r=(i,j)$
L	Fleet size of AVs
T	Number of time intervals in the planning horizon
x ¿$[x_{l,ij,t}]$	Decision variable for the routing and coverage problem (whether AV l traverses arc (i,j) at time step t)
y=$[y_{ij}]$	Decision variable in the routing and coverage problem (whether any AV traverses arc (i,j))
X_l	Space of feasible routes (solutions) for an AV l
$\overline{x}_{l,q}$	The q-th column (route candidate) for AV l
x_l	Route for AV l
$\lambda_{l,q}$	Weight given to the q-th column for AV l
Q_l	List of all columns (candidate routes) for AV l

Notation	Description
$\widetilde{Q}_l$	Revealed subset of columns (candidate routes) through column generation for AV l
$\overline{p}_{ij}$	Dual associated with the coverage check constraint for arc (i, j)
$\overline{v}_l$	Dual associated with convexity constraint for AVl
ζ_l	Minimum reduced cost among all extreme points of the subproblem for AV l

Appendix-III Research Outputs

Publication:

- Manuscript submitted to Transportation Research Part C: Emerging Technologies (Title: "Multi-source network-level pavement friction measurements via instrumented and dynamically routed autonomous vehicles")
- Manuscript accepted for presentation at 105th TRB Annual Meeting (Title: "Multi-Source Network-Level Pavement Friction Measurements via Instrumented and Dynamically Routed Autonomous Vehicles")
- Abstract accepted for presentation at 2025 INFORMS Annual Meeting (Title: "Routing autonomous vehicles to measure pavement friction in a network")
- Manuscript accepted for presentation at 2026 IEEE Intelligent Vehicles Symposium (Title: " High-Slip-Ratio Control for Peak Tire-Road Friction Estimation Using Automated Vehicles")

Appendix-IV Research Outcomes & Impacts

- This research has advanced roadway safety and asset management by integrating uncontrolled RV data with controlled AV-based active sensing to improve pavement friction estimation. The outcomes include:
    - Increased understanding and awareness - Transportation stakeholders now have greater awareness of the limitations of conventional friction measurement and the benefits of coordinated RV-AV sensing.
    - Growth of the knowledge base - New methods in high-slip-ratio AV control, nonlinear modeling, and sensor fusion expand the body of transportation research.
    - Improved processes and technologies - A structured framework for real-time, scalable friction mapping has been developed, enabling more accurate roadway condition monitoring.
    - Adoption potential - The approach demonstrates practical pathways for DOTs and policymakers to incorporate AVs into pavement management strategies.
    - Workforce development - The project trained graduate students and researchers in advanced modeling, optimization, and AV technologies.
- The impacts of this research extend to both practice and policy. For agencies, the framework enables more precise and timely identification of roadway segments with elevated crash risk, allowing maintenance and treatment resources to be prioritized where they will have the greatest safety benefit. By incorporating RVs and AVs into a cooperative sensing system, transportation networks can be monitored continuously without requiring large investments in new hardware. The framework also provides a foundation for integrating real-time friction data into broader asset management systems and decision-support tools. From a policy perspective, the results highlight the role of AVs not only as mobility providers but also as infrastructure monitoring assets, which may influence how state DOTs and metropolitan planning organizations regulate and collaborate with AV operators. In the long term, this research supports data-driven policymaking, promotes safer roadway conditions, and accelerates the adoption of innovative sensing and control technologies in transportation.

Reference

[1] H. Huang, J. Liu, Y. Yang, and J. Wang, 'Risk Generation and Identification of Driver-Vehicle-Road Microtraffic System', *ASCE. ASME. J. Risk Uncertain. Eng. Syst. A Civ. Eng.*, vol. 8, no. 3, p. 04022029, May 2022, doi: 10.1061/AJRUA6.0001199.

[2] C.-G. Wallman and H. Åström, 'Friction measurement methods and the correlation between road friction and traffic safety : A literature review', 2001, Accessed: Sep. 27, 2025. [Online]. Available: https://urn.kb.se/resolve?urn=urn:nbn:se:vti:diva-4541

[3] U. Department of Transportation, 'Federal Highway Administration Pavement Friction Management (PFM) Support Program PFM PROGRAM UTILIZING CONTINUOUS FRICTION MEASUREMENT EQUIPMENT AND STATE-OF-THE-PRACTICE SAFETY ANALYSIS DEMONSTRATION PROJECT FINAL REPORT', 2019, Accessed: Sep. 27, 2025. [Online]. Available: http://www.ntis.gov

[4] A. Elkhazindar, M. Hafez, K. K.- CivilEng, and undefined 2022, 'Incorporating pavement friction management into pavement asset management systems: State department of transportation experience', *mdpi.comA Elkhazindar, M Hafez, K KsaibatiCivilEng, 2022•mdpi.com*, Accessed: Sep. 27, 2025. [Online]. Available: https://www.mdpi.com/2673-4109/3/2/32

[5] J. Hu, S. Rakheja, and Y. Zhang, 'Real-time estimation of tire-road friction coefficient based on lateral vehicle dynamics', *journals.sagepub.comJ Hu, S Rakheja, Y ZhangProceedings of the Institution of Mechanical Engineers, Part D, 2020•journals.sagepub.com*, vol. 234, no. 10-11, pp. 2444-2457, Sep. 2020, doi: 10.1177/0954407020929233.

[6] B. Li, L. Zhang, C. Zhao, J. Lu, ... Q. M.-I. T., and undefined 2024, 'Capturing rapid vehicle dynamics: A refined adaptive kalman filter for enhanced tire-road friction estimation', *ieeexplore.ieee.orgB Li, L Zhang, C Zhao, J Lu, Q Meng, Z Zhang, H ChenIEEE Transactions on Industrial Electronics, 2024•ieeexplore.ieee.org*, Accessed: Sep. 27, 2025. [Online]. Available: https://ieeexplore.ieee.org/abstract/document/10472888/?casa_token=3o2-Ptoc0H8AAAAA:rHM6sr0DSGiskM8SJS-dmghp9wrtVJ0cBVSm7IcwT0Fs4lJ2zq9_chN3SG320j7KYT7hfDgcp_D0

[7] A. Kumar, T. Tang, A. Gupta, K. A.-C. S. in Construction, and undefined 2023, 'A state-of-the-art review of measurement and modelling of skid resistance: The perspective of developing nation', *ElsevierA Kumar, T Tang, A Gupta, K AnupamCase Studies in Construction Materials, 2023•Elsevier*, Accessed: Sep. 27, 2025. [Online]. Available: https://www.sciencedirect.com/science/article/pii/S2214509523003066

[8] R. McCarthy, ... G. F.-J. of T., and undefined 2021, 'Comparison and harmonization of the locked-wheel skid tester and the sideway-force coefficient routine investigation machine', *asmedigitalcollection.asme.orgR McCarthy, G Flintsch, E de León IzeppiJournal of Testing and Evaluation, 2021•asmedigitalcollection.asme.org*, Accessed: Sep. 27, 2025. [Online]. Available: https://asmedigitalcollection.asme.org/testingevaluation/article-abstract/49/6/3983/1191865

[9] J. W. Hall, K. L. Smith, L. Titus-Glover, J. C. Wambold, T. J. Yager, and Z. Rado, 'Web-Only Document 108: Guide for Pavement Friction National Cooperative Highway Research Program NCHRP ACKNOWLEDGMENT', 2009.

[10] S. B. Quiros, G. W. Flintsch, E. de L. Izeppi, and K. K. McGhee, 'Interconversion of locked-wheel and continuous friction measurement equipment (CFME) friction measurements', *journals.sagepub.comSB Quiros, GW Flintsch, EL Izeppi, KK McGheeTransportation Research Record, 2018•journals.sagepub.com*, vol. 2672, no. 40, pp. 452-462, Dec. 2018, doi: 10.1177/0361198118797455.

[11] F. Gustafsson, 'Slip-based tire-road friction estimation', *Automatica*, vol. 33, no. 6, pp. 1087-1099, 1997, doi: 10.1016/s0005-1098(97)00003-4.

[12] Y. Wang *et al.*, 'Tire road friction coefficient estimation: Review and research perspectives', *SpringerY Wang, J Hu, F Wang, H Dong, Y Yan, Y Ren, C Zhou, G YinChinese Journal of Mechanical Engineering, 2022•Springer*, vol. 35, no. 1, p. 6, Dec. 2022, doi: 10.1186/S10033-021-00675-Z.

[13] K. Singh, S. T.-S. S. & C. Engineering, and undefined 2015, 'Estimation of tire-road friction coefficient and its application in chassis control systems', *Taylor & FrancisKB Singh, S TaheriSystems Science & Control Engineering, 2015•Taylor & Francis*, vol. 3, no. 1, pp. 39-61, Jan. 2015, doi: 10.1080/21642583.2014.985804.

[14] J. Matuško, I. Petrović, and N. Perić, 'Neural network based tire/road friction force estimation', *Eng. Appl. Artif. Intell.*, vol. 21, no. 3, pp. 442-456, 2008, doi: 10.1016/j.engappai.2007.05.001.

[15] L. Alvarez, J. Yi, R. Horowitz, and L. Olmos, 'Dynamic friction model-based tire-road friction estimation and emergency braking

control', 2005, doi: 10.1115/1.1870036.

16] L. Cao, Y. Luo, Y. Wang, ... J. C.-J. of I. and, and undefined 2023, 'Vehicle sideslip trajectory prediction based on time-series analysis and multi-physical model fusion', *ieeexplore.ieee.orgL Cao, Y Luo, Y Wang, J Chen, Y HeJournal of Intelligent and Connected Vehicles, 2023•ieeexplore.ieee.org*, Accessed: Sep. 27, 2025. [Online]. Available: https://ieeexplore.ieee.org/abstract/document/10310059/

17] C. Tian, C. Huang, Y. Wang, ... E. C.-I. T., and undefined 2024, 'Recent estimation techniques of vehicle-road-pedestrian states for traffic safety: Comprehensive review and future perspectives', *ieeexplore.ieee.orgC Tian, C Huang, Y Wang, E Chung, AT Nguyen, PK Wong, W Ni, A Jamalipour, K LiIEEE Transactions on Intelligent Transportation Systems, 2024•ieeexplore.ieee.org*, Accessed: Sep. 27, 2025. [Online]. Available: https://ieeexplore.ieee.org/abstract/document/10814926/?casa_token=eQaEHfsxHUgAAAAA:uDYreNLNBRAAidLdjrrUm_aQKtiTfMhOt7gD4MUuJ_kK--7r5F8zXJmPabL3TUpm0t8n1hWi7A-7

18] F. Xiao, J. Hu, M. Jia, P. Zhu, C. D.- Measurement, and undefined 2022, 'A novel estimation scheme of tyre-road friction characteristics based on parameter constraints on varied-μ roads', *ElsevierF Xiao, J Hu, M Jia, P Zhu, C DengMeasurement, 2022•Elsevier*, Accessed: Sep. 27, 2025. [Online]. Available: https://www.sciencedirect.com/science/article/pii/S0263224122003426?casa_token=Grix0S0siuQAAAAA:gKY6a6ZRzMqGdgzTlJhoiAgS53d1o4Fz_vfEofQbnEY1gzgyaEgzrOhQPjH3jQqDe0MQzR_MDoPv

19] M. Ghorbani, A. Hosseinzadeh, M. Pirani, and A. Khajepour, 'Robust Transformer-Enhanced Tire Force Estimation: Combining Model-Based Observer and Deep Learning', 2025, doi: 10.36227/TECHRXIV.174286309.95198946.

20] T. Zhao, P. Guo, Y. W.-M. S. and S. Processing, and undefined 2024, 'Road friction estimation based on vision for safe autonomous driving', *ElsevierT Zhao, P Guo, Y WeiMechanical Systems and Signal Processing, 2024•Elsevier*, Accessed: Sep. 27, 2025. [Online]. Available: https://www.sciencedirect.com/science/article/pii/S0888327023009275?casa_token=WgSCGtM8I0oAAAAA:3A0e5DRBLsJ9jpCK2FSErLVV1oCTC2iOcCd4N0tlRrMVtlj4BSdXq0dJS1Hq9D2gnqJ0Bl1_UfeF

21] S. M. ller, M. U.-J. Dyn. Sys., undefined Meas, and undefined 2003, 'Estimation of the maximum tire-road friction coefficient', *asmedigitalcollection.asme.orgS Mu¨ ller, M Uchanski, K HedrickJ. Dyn. Sys., Meas., Control, 2003•asmedigitalcollection.asme.org*, 2001, doi: 10.1115/1.1636773.

22] C. Canudas-De-Wit, R. H.-P. of the 38th IEEE, and undefined 1999, 'Observers for tire/road contact friction using only wheel angular velocity information', *ieeexplore.ieee.orgC Canudas-De-Wit, R HorowitzProceedings of the 38th IEEE Conference on Decision and Control, 1999•ieeexplore.ieee.org*, Accessed: Sep. 27, 2025. [Online]. Available: https://ieeexplore.ieee.org/abstract/document/827973/?casa_token=QHlVnXsg9soAAAAA:HNo9oGESzoootnD560LCBFCXz-sEdlKIkDcQj8D2oz-e9mXZ9qjPVoaP0UdYSstStH8uXlTcbVAS

23] H. Yiğit, H. Köylü, S. E.-E. S. with Applications, and undefined 2023, 'Estimation of road surface type from brake pressure pulses of ABS', *ElsevierH Yiğit, H Köylü, S EkenExpert Systems with Applications, 2023•Elsevier*, Accessed: Sep. 27, 2025. [Online]. Available: https://www.sciencedirect.com/science/article/pii/S095741742201747X?casa_token=mySFGWrg5j0AAAAA:dAqWOFMPg7pmGYZlI6IHJitHf4LUWYSKRLYTTAUwLz1liuGl8vHp0ECjK47TMzSWcETPLvZsx7TP

24] H. B. Pacejka and E. Bakker, 'THE MAGIC FORMULA TYRE MODEL', *http://dx.doi.org/10.1080/00423119208969994*, vol. 21, no. sup1, pp. 1-18, Jan. 2007, doi: 10.1080/00423119208969994.

25] R. Rajamani, G. Phanomchoeng, D. Piyabongkarn, and J. Y. Lew, 'Algorithms for real-time estimation of individual wheel tire-road friction coefficients', *IEEE/ASME Transactions on Mechatronics*, vol. 17, no. 6, pp. 1183-1195, 2012, doi: 10.1109/TMECH.2011.2159240.

26] 'Seber, G. A. F. and C. J. Wild, Nonlinear Regression.... - Google Scholar'. Accessed: Sep. 29, 2025. [Online]. Available: https://scholar.google.com/scholar?hl=en&as_sdt=0%2C50&q=Seber%2C+G.+A.+F.+and+C.+J.+Wild%2C+Nonlinear+Regression.+John+Wiley+%26+Sons%2C+2003.&btnG=

27] R. B.-P. Review and undefined 1932, 'The calculation of errors by the method of least squares', *APSRT BirgePhysical Review, 1932•APS*, vol. 40, no. 2, pp. 207-227, 1932, doi: 10.1103/PHYSREV.40.207.

28] R. Tegge, J. J.-I.-10-066 UILU-ENG-2010-2006, and undefined 2010, 'Development and application of safety performance functions for Illinois', *ideals.illinois.eduRA Tegge, JH JoICT-10-066 UILU-ENG-2010-2006, 2010•ideals.illinois.edu*, 2010, Accessed: Sep. 29, 2025. [Online]. Available: https://www.ideals.illinois.edu/items/45954

[29] S. L.-J. of safety research and undefined 2011, 'Efficacies of roadway safety improvements across functional subclasses of rural two-lane highways', *Elsevier*, Accessed: Sep. 29, 2025. [Online]. Available: https://www.sciencedirect.com/science/article/pii/S0022437511000570?casa_token=5AH99uptPWQAAAAA:RfQp8qUkFMLCywJMr2uUX9hw7Lk8bWZpGz_DgHUSvQwyohDhx3WRFGRKqopYZZEvst0GcEN-9OyJ

[30] Y. Chen, B. P.-A. A. & Prevention, and undefined 2014, 'Methodology to develop crash modification functions for road safety treatments with fully specified and hierarchical models', *ElsevierY Chen, B PersaudAccident Analysis & Prevention, 2014•Elsevier*, Accessed: Sep. 29, 2025. [Online]. Available: https://www.sciencedirect.com/science/article/pii/S0001457514000785?casa_token=5JIPwP9d05YAAAAA:PYZaDrA9HwWEewkyFipUi4PsrsB4vi4yBp6W2hcSKghxpFIKXowfIYTYpxyh624QEq4-rvhvwv1s

[31] E. Hauer, 'Statistical Road Safety Modeling', *Transp. Res. Rec.*, no. 1897, pp. 81-87, 2004, doi: 10.3141/1897-11.

[32] D. Lord, F. M.-T. research part A. policy and practice, and undefined 2010, 'The statistical analysis of crash-frequency data: A review and assessment of methodological alternatives', *ElsevierD Lord, F ManneringTransportation research part A: policy and practice, 2010•Elsevier*, Accessed: Sep. 29, 2025. [Online]. Available: https://www.sciencedirect.com/science/article/pii/S0965856410000376?casa_token=93MCTei3_wQAAAAA:dns0D9ByRjIrNpp8MX9H0W2mspP2t1TMMrCkLNUJT4rnLMEcchsUFMo3EvgUg-iRfuR-2Bjcg701

[33] W. CAN, O. L.- BioScience, and undefined 2001, 'Log-normal Distributions across the Sciences: Keys and Clues', *statpower.net*, 2001, Accessed: Sep. 29, 2025. [Online]. Available: https://statpower.net/Content/MLRM/Readings/LimpertStahelAbt2007.pdf

[34] G. B. Dantzig and P. Wolfe, 'Decomposition Principle for Linear Programs', *https://doi.org/10.1287/opre.8.1.101*, vol. 8, no. 1, pp. 101-111, Feb. 1960, doi: 10.1287/OPRE.8.1.101.

[35] B. Kallehauge, J. Larsen, O. B. G. Madsen, and M. M. Solomon, 'Vehicle Routing Problem with Time Windows', *Column Generation*, pp. 67-98, 2005, doi: 10.1007/0-387-25486-2_3.

[36] A. K.-C. of the ACM and undefined 1962, 'Topological sorting of large networks', *dl.acm.orgAB KahnCommunications of the ACM, 1962•dl.acm.org*, vol. 5, no. 11, pp. 558-562, Nov. 1962, doi: 10.1145/368996.369025.

[37] C. Barnhart, E. L. Johnson, G. L. Nemhauser, M. W. P. Savelsbergh, and P. H. Vance, 'Branch-and-price: Column generation for solving huge integer programs', *pubsonline.informs.orgC Barnhart, EL Johnson, GL Nemhauser, MWP Savelsbergh, PH VanceOperations research, 1998•pubsonline.informs.org*, vol. 46, no. 3, pp. 316-329, 1998, doi: 10.1287/OPRE.46.3.316.

[38] M. B.-T. Science and undefined 1983, 'The estimation of an origin-destination matrix from traffic counts', *pubsonline.informs.orgMGH BellTransportation Science, 1983•pubsonline.informs.org*, vol. 17, no. 2, pp. 198-217, 1983, doi: 10.1287/TRSC.17.2.198.

[39] Q. Huangfu, J. H.-M. P. Computation, and undefined 2018, 'Parallelizing the dual revised simplex method', *SpringerQ Huangfu, JAJ HallMathematical Programming Computation, 2018•Springer*, vol. 10, no. 1, pp. 119-142, Mar. 2018, doi: 10.1007/S12532-017-0130-5.